

**PREDICTING PROPERTIES OF PROTEINS AND POLYMERS BY COARSE-
GRAINED METHODS AND USING NANOPROBES**

by

İBRAHİM İNANÇ

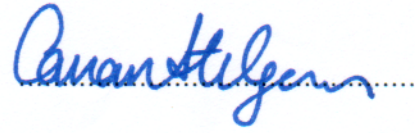
**Submitted to the Graduate School of Engineering and Natural Sciences
in partial fulfillment of
the requirements for the degree of
Doctor of Philosophy**

**Sabancı University
Spring 2011**

PREDICTION OF PROPERTIES OF PROTEINS AND POLYMERS BY
COARSE- GRAINED METHODS AND USING NANOPROBES

APPROVED BY

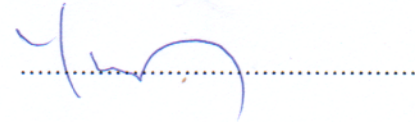
Prof. Canan Atilgan
(Thesis Supervisor)



Prof. Ali Rana Atilgan
(Thesis Coadvisor)



Prof. Yusuf Mencilođlu



Assoc. Prof. Melih Papila



Assoc. Prof. Mustafa M. Demir



DATE OF APPROVAL: 09.08.2011

© İbrahim İnanç 2011

All Rights Reserved

ABSTRACT

The past decade has witnessed the development and success of coarse-grained network models of proteins for predicting many equilibrium properties related to collective modes of motion. Curiously, the results are usually robust towards the different methodologies used for constructing residue networks from knowledge of the experimental coordinates. In the first part of the thesis, we present a systematical study of network construction strategies, and we study their effect on the predicted properties using Anisotropic Network Model (ANM). The analysis is based on the radial distribution function and the spectral dimensions of a large set of proteins as well as a newly defined quantity, the angular distribution function. In the second part of the study, we apply ANM to the well-relaxed atomistic coordinates of a 32-chain C128 *cis*-1,4-polybutadiene system to test the extent of applicability of the method. 15-60 ns long molecular dynamics (MD) simulations are carried out for a wide variety of temperatures and pressures. The mean-square fluctuations of the central carbon atoms obtained by applying ANM on a few snapshots are shown to be in good agreement with values from full MD simulations. This leads to predict average flexibility values of the system under different conditions. We extend the methodology to approximate the virial of the system. In the third part, to understand the nanoclusters' behavior and influence on the polymer's viscoelastic and thermodynamic properties, different nanoclusters having 10 to 150 atoms are embedded in the *cis*-1,4-polybutadiene matrix. First, the diffusion coefficient and zero shear viscosity are calculated from the simulations and compared with the experimental results obtained with rotational viscosimeter. In addition, correlation times of C-H bond vectors of simulation at four different temperatures were compared with the C-NMR experiments of *cis*-1,4-polybutadiene with high-*cis*-content polybutadiene (%93 *cis*, %3 *trans* and %4 *vinyl*). The agreement between simulation results and experiments confirm that the united atom force field used in the simulations well-describes the dynamics of the real system. It is also possible to manipulate mechanical properties by tuning the interaction strength of the nanoclusters with the chains. From a practical point of view, we can assume that bulk modulus is not much affected by the size of the nanocluster, whereas it linearly increases as the interaction strength changes from normal to strong. Another thermodynamical quantity, glass transition temperature (T_g) increases from ~176 K to ~184 K as the nanoclusters are introduced to the polymer melt. T_g decreases to ~178 K as their interaction strength is made much stronger than the standard value.

ÖZET

Geçtiğimiz on yılda toplu hareket modları ile ilgili pek çok denge özelliğini tahmin etmek için proteinlerde kaba-ölçekli ağ modelleri geliştirilip başarılı bir şekilde uygulanmıştır. Deneysel kordinat bilgilerinden ağlar oluşturularak kullanılan farklı yöntemler genellikle iyi sonuçlar vermektedir. Tezin ilk bölümünde, ağ örgüleme stratejilerinin sistematik bir çalışması ve Anizotropik Ağ Modeli (AAM) kullanılarak tahmin edilen özellikler üzerindeki etkisi araştırıldı. Analizler çok sayıdaki proteinin ortak radyal dağılım fonksiyonu, bu tezde tanımlanan açılal dağılım fonksiyonu ve spektral boyuta dayanmaktadır. Çalışmanın ikinci bölümünde ise, 32-zincirli 128 carbon atomundan oluşan *cis*-1,4-polibütadien eriyik sisteminin denge koşullarındaki atomlarının koordinatlarına AAM uygulanmıştır ve yöntemin uygulanabilirliği test edilmiştir. 15-60 ns uzunluğundaki molekül dinamik (MD) benzetimleri geniş bir sıcaklık ve basınç aralığında yapılmıştır. Bir kaç anlık görüntüye AAM uygulanarak elde edilen merkezi karbon atomlarının ortalama kare dalgalanmalarının MD benzetim değerleri ile uyumluluk içerisinde olduğu gösterilmiştir. Bu değerler, sistemin farklı koşullar altında ortalama esneklikleri tahmin etmek için kullanılmıştır. Ayrıca, uygulanan metod sistemin yaklaşık viral değerlerini elde etmek için genişletilmiştir. Üçüncü bölümde, nanoparçacıkların polimerin viskoelastik ve termodinamik özellikleri üzerindeki davranış ve etkisini anlamak için, 10 ila 150 atomdan oluşan farklı büyüklükteki nanoparçacıklar *cis*-1,4-polibütadien matrisi içerisinde çalışılmıştır. İlk olarak, difüzyon katsayısı ve sıfır kayma viskozitesi betimleme sonuçlarından hesaplanmış ve dönme viskozimetre ile elde edilen deney sonuçları ile karşılaştırılmıştır. Buna ek olarak, dört farklı sıcaklıkta hesaplanan C-H bağ vektörlerinin korelasyonları yüksek *cis* yapıdaki polibütadienden elde edilmiş C-NMR deneyleri ile karşılaştırılmıştır. Benzetim sonuçları ve deneyler arasında uyumluluk kullanılan birleşik atom kuvvet alanının gerçek sistem dinamiklerini iyi şekilde betimlediğini onaylamaktadır. Zincirler ile nanoparçacıklar arasındaki etkileşim gücünü değiştirerek polimerin mekanik özelliklerini de değiştirmek mümkündür. Esneklik modülü etkileşimi normalden çok güçlüye değiştirdikçe doğrusal olarak artmakta, oysa ki, pratik anlamda nanoparçacık boyutundan etkilenmemektedir. İncelenen diğer bir termodinamik özellik olan camsı geçiş sıcaklığı ise nanoparçacıklar sisteme entegre edilince ~176 K'den ~ 184 K'e artış göstermekte, ancak etkileşim standart değerlerin çok üzerindeki güçlü değerlerde uygulanınca tekrar nanoparçacıksız durumdaki yalın polimer değerine yakın (~ 178 K) düşmektedir.

“To my family”

ACKNOWLEDGEMENTS

It is a great pleasure to work under supervision of Prof. Canan Atılğan and Prof. Ali Rana Atılğan. I would like to express my deepest gratitude to my thesis advisors for their invaluable guidance, motivation and endless encouragement throughout this study. I will always be thankful to their advices and support throughout my thesis work.

I also would like to thank to the thesis committee members: Prof. Yusuf Mencelođlu, Assoc. Prof. Melih Papila, Assoc. Prof. Mustafa Demir for their invaluable comments and review on the thesis.

All of my friends made me have a great working time in Sabancı University. I specially thankful to Dr. Burcu Saner, Cahit Dalgıçtır, Dr. Çınar Öncel, Dr. Deniz Turgut, Dr. Engin Karabudak, Eren Şimşek, Gökhan Kaçar, Dr. Mehmet Özdemir, Murat Mülayım, Osman Burak Okan, Dr. Özgür Bozat, Özlem Sezerman and other MAT graduate students for their friendship and support.

Finally, I would like to acknowledge Sabancı University, Academic Support Program (ASP) and Turkish Scientific and Technological Research Council (TÜBİTAK) for giving scholarship throughout my education.

TABLE OF CONTENTS

ABSTRACT.....	iv
ACKNOWLEDGEMENTS.....	vii
TABLE OF CONTENTS.....	viii
LIST OF FIGURES.....	x
LIST OF TABLES.....	xii
LIST OF SYMBOLS.....	xiii
LIST OF ABBREVIATIONS.....	xiv
1. INTRODUCTION.....	15
1.1. Residue Network Construction and Predictions of Elastic Network Model.....	18
1.2. Properties of Polybutadiene Melts Probed by Nanoclusters.....	20
1.3. General Approach.....	22
2. THEORETICAL BACKGROUND AND METHODS.....	25
2.1. Theory.....	25
2.1.1. Radial and angular distribution functions.....	25
2.1.2. From $g(r)$ to thermodynamic relations.....	27
2.1.3. Prediction of the effective intermolecular potential $u(r)$	28
2.1.4. Anisotropic network model as a coarse-grained method.....	29
2.2. Methods and Systems Studied.....	30
2.2.1. Molecular dynamics (MD) simulation.....	30
2.2.2. Molecular modeling and simulation details for PBD melts.....	32
2.2.3. Network construction from PBD melt simulations.....	35
2.2.4. Simulation details for PBD melts with nanoprobess.....	36
2.2.5. Network construction from proteins and protein data sets.....	38
2.2.6. Viscosity measurement experiments.....	39
2.3. Properties Calculated.....	39
2.3.1. Diffusion coefficient and zero-shear viscosity calculations.....	39
2.3.2. Dynamical properties.....	40
2.3.3. Mechanical properties.....	41
2.3.4. Glass transition temperature.....	44

3. RESIDUE NETWORK CONSTRUCTION AND PREDICTION OF ELASTIC NETWORK MODELS	45
3.1. Structural Heterogeneity of Amino acid Distributions in Proteins.....	45
3.2. Density of Vibrational Normal Modes.	46
3.3. Biological Significance.....	49
4. PREDICTION OF THERMODYNAMICS MEASURABLES OF CIS-1,4-POLYBUTADIENE.....	51
4.1. Thermodynamical and Structural Properties	51
4.2. Thermal Fluctuations	54
4.3. Predicting the Second Virial Coefficients	56
5. LINEAR VISCOELASTIC PROPERTIES OF POLYBUTADIENE MELTS PROBED BY NANOCCLUSERS: MD SIMULATIONS AND EXPERIMENTS	58
5.1. Radial Distribution Function (RDF) of Polymer with Nanoclusters.....	58
5.2. Diffusion Coefficient and Zero-Shear Viscosity	58
5.3. Dynamical Properties	60
5.4. Mechanical Properties	62
5.5. Glass Transition Temperature	64
6. CONCLUSION AND FUTURE WORK	66
APPENDICES	70
APPENDIX A: Application of Periodic Boundary Conditions (PBC).....	70
APPENDIX B: Derivation of Second Virial Coefficient (b_2) from ANM.....	71
APPENDIX C: Derivation of Isothermal Compressibility (κT) from ANM	72
APPENDIX D: Details of the Diffusion Coefficients and Viscosity Predictions.....	73
REFERENCES	75

LIST OF FIGURES

Figure 2.1. (a) The negative of the resultant vectors acting on the nodes, $-\mathbf{Q}_i$, exemplified by a 54 residue protein (PDB code: 1enh). (b) Part of the helix marked by the square in (a) is magnified; “exterior” refers to the solvent contacting part of the helix, and “interior” marks the side facing the core of the protein.

Figure 2.2. United-atom model representation of *cis*-1,4-PB

Figure 2.3. RMS-fluctuations obtained from ANM for different cut-off values ($r_{cut}=7.5 \text{ \AA}$, 10 \AA and 12.5 \AA).

Figure 2.5. Mean square displacements vs. time for diffusion coefficient calculation

Figure 2.6. Graphical schema of volume-temperature curves for crystalline and amorphous polymer

Figure 3.1. (a) Radial and angular distribution functions (left y-axis: RDF; right y-axis: ADF) obtained by averaging over 595 proteins. (b) ADFs computed separately for the core and surface residues for a subset of 60 proteins

Figure 3.2. (a) The change of the density of vibrational modes, $g(\omega)$, with the cut-off distance, r_c , used in network construction. (b) Spectral dimension, d_s , of the networks, obtained from power law best-fits to the cumulative density of modes, $G(\omega) \propto \omega^{d_s}$ for the first 70 modes in each set of data.

Figure 3.3. (a) Comparison of the X-ray B-factors (gray, middle curve) with fluctuation profiles predicted from various models (b) Pearson correlation coefficients at a wide range of cut-off distances for the same protein

Figure 4.1. (a) Temperature dependence of isothermal compressibility (κ_T) and (b) specific volume (v) at 1 atm obtained from MD simulations

Figure 4.2. Characteristic ratio of the *cis*-1,4-PB obtained from MD simulations at different temperatures.

Figure 4.3. Radial distribution function (RDF) of 14 sets of simulation

Figure 4.4. Normalized RMSD averaged over all chains obtained from ANM and MD simulation for different temperatures at 1 atm, 1000 atm and for different pressures at 380 K.

Figure 4.5. Pearson correlation factors, r , of chain fluctuations calculated from MD simulations and ANM

Figure 4.5. Comparison of spring constants for different (a) temperature and (b) pressure sets.

Figure 4.6. Normalized second virial coefficients at (a) constant pressure of 1 atm, (b) constant pressure of 1000 atm, (c) and at constant temperature of 380 K

Figure 5.1. Comparison of RDF of sp^3 and sp^2 atoms at $T=330$ K

Figure 5.2. Cluster size effect on the RDF of sp^3 and sp^2 atoms at $T=330$ K

Figure 5.3. Effect of temperature to the RDF of sp^3 and sp^2 atoms for the system with nanocluster of 10 atom-size

Figure 5.4. Comparison of zero-shear viscosity with respect to temperature obtained from simulations and experiment

Figure 5.5. Comparison of correlation time, τ_c , of simulation and experiment with respect to temperature calculated from probes of $N = 10$

Figure 5.6. (a) Temperature and (b) size dependence of residence times (τ_r)

Figure 5.7. (a) Effect of vdw interaction strength to τ_r and (b) τ_c at $T=330$ K and $N=150$

Figure 5.8. (a) Effect of cluster size, (b) and vdw interaction strength to bulk modulus calculated from inverse of κ_T

Figure 5.9. Effects of vdw interaction strength, MW to bulk modulus that are calculated from inverse of κ_T

Figure 5.10. Effect of (a) molecular weight, (b) nanocluster size, and (c) vdw interaction strength on shear modulus

Figure 5.11. Change in specific volume with respect to temperature for predicting T_g

Figure 5.12. Change in specific volume with respect to MW for $-\epsilon_{Si-C} = 1.5$ kcal/mol (strong vdw interaction)

Figure A.1. Graphical representations of Free Boundary (FB) and Periodic Boundary Conditions (PBC) and corresponding Connectivity Matrices

Figure D.1. Predictions of zero-shear viscosities from diffusion coefficients for temperatures, 330 K, 380 K, and 430 K

LIST OF TABLES

Table 2.1. Summary of MD Simulations at the data collection stage

Table 2.2. Force-field parameter of united-atom model used for MD simulations

Table 2.3. Overview of the simulations for 32 PBD chains of 32 repeat units

Table 4.1. Second virial coefficients obtained from RDF and ANM construction

Table D.1. Details of the diffusion coefficients of PBD+Cluster at $T=330$ K

Table D.2. Details of the diffusion coefficients of PBD+Cluster at $T=380$ K

Table D.3. Details of the diffusion coefficients of PBD+Cluster at $T=430$ K

LIST OF SYMBOLS

b_2	second virial coefficient
$\epsilon_{\text{Si-C}}$	vdw interaction strength
Γ	Kirchhoff matrix
k_B	Boltzmann constant
κ_T	isothermal compressibility
λ	thermal <i>de Broglie</i> wavelength
η	intrinsic viscosity
η_0	zero shear viscosity
ρ	density
ζ	coupling parameter
τ_c	correlation time
τ_r	residue time
C_n	characteristic ratio
D	diffusion coefficient
E	Young Modulus
G	Shear Modulus
H	Hessian Matrix
K	Bulk Modulus
N	number of particles
R_g	radius of gyration
$u(r)$	effective intermolecular potential
T	temperature
T_g	glass transition temperature
vdw	van der Waals

LIST OF ABBREVIATIONS

ADF	Angular Distribution Function
ANM	Anisotropic Network Model
GNM	Gaussian Network Model
MD	Molecular Dynamics
MS	Materials Studio
MW	Molecular Weight
NMA	Normal Mode Analysis
NMR	Nuclear Magnetic Resonance
NPT	Isothermal-Isobaric
PB	Polybutadiene
PBC	Periodic Boundary Conditions
PDB	Protein Data Bank
RDF	Radial Distribution Function
RMSD	Root Mean Square Displacement
XRD	X-ray Diffraction

1. INTRODUCTION

Soft materials science, focusing on such versatile materials as proteins, polymers, self-assembled micellar structures, complex fluids, liquid crystals, elastomers, soft ferroelectric materials, foams, and gels, is an active area of scientific research and technological applications. Soft matter plays a role in a wide variety of important processes and applications, as well as in all living systems. Due to their complex nature, understanding and controlling the behavior of soft materials through the relationship between their structures, dynamics and function requires an interdisciplinary approach using theoretical models, complementing computational and experimental findings. The ultimate goal is to engineer and design materials with specific functions having the desired macroscopic mechanical, thermal and dynamical properties by selectively manipulating microscopic parameters such as chemical composition, or choice of interacting species. To reach such goals, studying the equilibrium and dynamical properties of proteins that provide excellent models for self-assembled polymeric materials proves useful.

The physical properties of polymers starting from basic structure information was pioneered by Flory and others in the late 1940s [1]. Despite the limitations of Flory-Huggins theory for the thermodynamics of macromolecules, such as its use of a lattice model, random mixing, and incompressibility assumptions, it is still useful in understanding and predicting the qualitative behavior of polymer solutions, melts and mixtures. Recently other theoretical methods, including scaling arguments [2] and renormalization group theory [3], enabled a more thorough understanding of the polymer properties and behavior on larger length scales [4]. According to these theories, many important properties of polymeric systems are not universal, but rather depend on the details of local packing and to the specific architecture of the polymer. For example, the dynamics of linear polymer chains in the melt depends strongly on chain length: for short, unentangled chains, the dynamics is determined by a balance of viscous and entropic forces; for long chains, topological constraints are more dominant [1].

In addition to theoretical and experimental developments, classical atomistic simulations, in particular molecular dynamics (MD) simulations [5], have become a

common tool for investigating the properties of polymer and biomolecular systems in the last decades. Because of their remarkable single atom resolution, femtosecond time scales, and more realistic energetic environment, MD simulations assist experimental techniques by providing insight into observed processes [6]. MD simulations, basically an integration of the classical equations of motion, generating the trajectory of configuration space in time, can provide detailed information on the behavior at the atomistic level, but are generally limited to time scales up to the order of hundreds of nanoseconds, which is not enough to explain many interesting phenomena occurring on the order of seconds. The technique of dissipative particle dynamics (DPD) was introduced by Hoogerbrugge and Koelman in order to fill the gap between the atomistic simulation methods and continuum fluid models without applying lattice models [7]. DPD uses group of atoms called “beads” moving via classical equations of motion, interacting by soft potentials and predefined collision rules. The momentum of the interacting blocks is conserved providing a hydrodynamic solution for the system. After the formulation of the underlying physics using statistical mechanics and mapping bead interactions onto Flory-Huggins mean field theory of polymers by Espanol and Warren [8], many polymeric systems such as polymer melts [9] and polymer chains [10, 11], block copolymers [12, 13], and random elastomers [14, 15] have been investigated by DPD. The results were found to be in good agreement with other theories and experiments, and provides a route for generating initial morphologies for further use in multi-scale approaches [16].

Alternative coarse-grained models have been developed to study properties of proteins. Globular proteins show diversified structures and sizes, yet, it has been claimed that they display a nearly random packing of amino acids with strong local symmetry on the one hand [17], and that they are regular structures that occupy specific lattice sites, on the other [18]. It was later shown that this classification depends on the property one investigates, and that proteins display “small-world” properties, where highly ordered structures are altered with few additional links [19]. Furthermore, packing density of proteins scales uniformly with their size [20, 21] which causes them to show similar vibrational spectral characteristics to those of solids [22].

Dynamical studies of folded proteins draw much attention to their importance in relating the structure of the proteins to their specific function and collective behavior.

Protein dynamics is generally both anisotropic and collective. Internal motional anisotropy is a consequence of the general lack of symmetry in the local atomic environment, while the collectivity is mainly caused by the dense packing of proteins [23].

Theoretical studies on fluctuations and collective motions of proteins are based on either molecular dynamics (MD) simulations or normal mode analysis (NMA). Since, in molecular simulations with conventional atomic models and potentials, computational effort is demanding for larger proteins with more than a few hundreds of residues, coarse grained protein models with simplified governing potentials have been employed. Of these, Anisotropic Network Model (ANM) in particular, has shown great success in the description of the residue fluctuations and the collective behavior of proteins [24-26].

While heterogeneity is ever-present in proteins leading to the specific functions carried-out in the cell environment, it may be created in polymers in a plethora of ways. These include polymer mixtures, copolymers, using different solvents as well as including nanofillers to obtain various properties of interest. In this work, we shall be mainly interested in the latter because it poses an open problem. While it is clear that the interfacial region between the nanofiller and the polymeric chains has a significant impact on the properties of nanocomposites, quantitative understanding of the structure and morphology of the polymer interacting with nanoscale surfaces is still developing. Together with dynamical and mechanical analysis, rheology is extensively used in nanoscale composites to probe the extent, structure, and properties of the interfacial region [27] and it has been found that the extent and properties of the interfacial region depend on the nanofiller/matrix interactions. In this work, the effect of nanofiller interaction strength as well as nanofiller size on mechanical and thermodynamical properties is systematically studied for the first time in the literature.

In this thesis, we shall first study the extent of predictions of elastic network models on the well-studied protein systems. We shall then seek to understand the extent of applicability of ANM to oligomeric systems, exemplified by polybutadiene melts. We shall then use nanoclusters to probe the linear viscoelastic properties of the melts. Finally, we shall use these nanoprobables to manipulate properties of polymers. These include mechanical strength, which is directly related to force constants derived by

ANM, as well as the glass transition temperature, which is shown to be both upshifted and restored by playing with van der Waals (vdw) interaction strength.

1.1. Residue Network Construction and Predictions of Elastic Network Model

NMA using a single parameter harmonic potential [28] successfully predicts the large amplitude motions of proteins in the native state [29]. Within the framework of this model, proteins are modeled as elastic networks whose nodes are residues linked by inter-residue potentials that stabilize the folded conformation. The residues are assumed to undergo Gaussian-distributed fluctuations about their native positions. The springs connecting each node to all other neighboring nodes are of equal strength, and only the atom pairs within a cut-off distance are considered without making a distinction between different types of residues. This model, with its simplicity, speed of calculation and relying mostly on geometry and mass distribution of the protein, demonstrates that a single-parameter model can reproduce complex vibrational properties of macromolecular systems. By separating different components of normal modes, e.g. collective (low-frequency) motions, the nature of a conformational change, for example due to the binding of a ligand, can also be analyzed thoroughly [30].

Following the uniform harmonic potential introduced originally by Tirion [31], residue level application of elastic network models paved the way for the concept Gaussian Network Model (GNM), which is based on the energy balance of the system at the energy minimum, and is a purely thermodynamic treatment [29, 32]. Elastic models based on the force balance around each node [33] led to the development of the ANM [24]. In the past few years, variant methods of GNM and ANM [34, 35] have been introduced. The applications of these models to many proteins show successful results in terms of predicting the collective behavior of proteins. Despite numerous applications comparing the theoretical and experimental findings on a case-by-case basis [36-40], only a few attempted a statistical assessment of the models. A methodology that evaluates the number of modes necessary to map a given conformational change from the degree of accuracy obtained by the inclusion of a given number of modes, showed the results to be protein dependent [41]. In another study where 170 pairs of structures were systematically analysed, it was shown that the

success of coarse-grained elastic network models may be improved by recognizing the rigidity of some residue clusters [42].

To date, the structures that form the basis of the network models have been generated from certain rules of thumb. In GNM, which does not include directionality and is therefore a one-dimensional model, the first correlation shell between the C_α or C_β atoms of the residues is used as the rule for the connectedness of a given pair of residues (ca. 6.7 – 7.0 Å) [29]. In the three-dimensional ANM, values in the range of 8 – 14 Å are found in the literature based on the argument that (i) the eigenvalue distributions obtained from the modal decomposition are similar to those obtained from the full-atom NMA description of proteins, or (ii) these provide atomic fluctuation profiles that display the largest correlation with the experimental B-factors. Voronoi tessellation of the space defined by the central (usually C_α or C_β) atom into non-intersecting polyhedra constitute another route that frees one from defining a cut-off distance [43]. Atom-based network construction approaches have also been used. A review of the variety of network construction methods published by Csermely *et al.* is also available in the literature [44].

In this thesis, we use a systematic approach on a large set of globular proteins with varying architectures and sizes to find a basis for why the network models work well to define certain properties of the system. This enables us to assess the various residue-based approaches used in the construction of the networks. We define a direction based radial distribution function for this purpose, and show that the orientation of newly added links samples a spherically symmetric collection of directions beyond a given distance of interacting residues. We show that the network construction is free of the cut-off distance problem once a certain baseline threshold is accessed, if one is interested in the collective motions and the fluctuation patterns of the residues. Implications for the limitations of the ANM methodology are also discussed due to functionality-related predictions based on the most global motions.

1.2. Properties of Polybutadiene Melts Probed by Nanoclusters

Polymer nanocomposites are polymer matrix composites in which the fillers are less than 100 nm in at least one dimension. These composites have exhibited extraordinary properties such as increasing the elastic moduli by an order of magnitude while maintaining glass transition temperature [45]. A defining feature of polymer nanocomposites is that the small size of the fillers leads to a dramatic increase in interfacial area as compared to traditional composites. This interfacial area creates a significant volume fraction of interfacial polymer with properties different from the bulk polymer even at low loadings. The properties and structure of this interfacial region are not yet known quantitatively, presenting a challenge both for controlling and predicting the properties of polymer nanocomposites.

One of the challenges in developing polymer nanocomposites for advanced technology applications is a limited ability to predict the properties. While the techniques exist to tailor the surface chemistry and structure of nanoparticle surfaces [46], the impact of the nanoscale filler surface on the morphology, dynamics, and properties of the surrounding polymer chains cannot be quantitatively predicted. Therefore, the properties of a significant volume fraction of the polymer, the interfacial polymer, are unknown, making it difficult to predict bulk properties. One of the challenging goals in nanocomposite science is to fully understand the impact of the interfacial region on both composite properties and to have the ability to model behavior of nanocomposites

The structure and properties of the interfacial region are not only different from the bulk, but are also critical in controlling properties of the overall nanocomposite. Since the interfacial region properties must play a significant role in increasing the composite modulus, for amorphous polymer matrices, it is hypothesized that the interfacial region in the nanotube composites is a region of polymer with reduced mobility and associated higher stiffness [47, 48].

In amorphous polymer matrices, it is qualitatively understood that an attractive interface will decrease the mobility of the polymer chains and a repulsive interface will increase the mobility [49]. One method for probing this change in mobility of the

polymer chains in the interfacial region is to measure the glass transition temperature, using either differential scanning calorimetry or rheology typically dynamic mechanical analysis [50, 51]. Studies using these methods show that the glass transition temperature of a polymer nanocomposite can be raised or lowered with the addition of nanoparticles with attractive and repulsive interaction with the matrix, respectively [52, 53].

Recent experiments have helped demonstrate that nanoscopic additives can alter the properties of polymeric materials in several important ways. The elastic constants, the toughness, and the modulus at frequencies below the end of the plateau modulus of the composite can be very different from those of the pure polymer [27, 54, 55]. Depending on the nature of the interactions between the nanoparticles and the polymer matrix, the plateau modulus can either increase [54] or decrease [27] suggesting that the addition of these particles modifies the properties of the polymer matrix in unanticipated ways.

Although experimental work [56, 57] points to a reduction in molecular mobility in the region of the interface, little is known about the origin of this immobilization. It is experimentally challenging to generate equilibrated, well-dispersed homogeneous nanoparticle/polymer samples, rendering it difficult to establish general principles regarding the manner in which nanoparticles affect polymer properties. So, it is more efficient to undertake a study of a nanocomposite system using a molecular modeling approach. The structure and dynamics of the nanoparticle-polymer matrix interface have only recently started to become studied using such simulation techniques [58-61]. Bitsanis et al. [62] give a review of some of the early work in the field and describe their MD simulations of liquid systems of relatively short freely jointed chains in the vicinity of a plain wall. Beside these MD simulations. Binder and co-workers have used dynamic MC simulations using the bond-fluctuation lattice model to study similar systems using an even more coarse-grained approach [63, 64].

Until now, several hypotheses have been proposed to rationalize the reinforcement of polymeric materials by nanoparticles. These include interaction zone arguments, originally put forth to explain experimental results [65] and, more recently, supported by molecular simulations [66]. Such arguments propose that a layer near the surface of the particles exhibits dramatically different properties than those of the bulk material [67, 68] . Some experimental studies have speculated that the density of

entanglements near the surfaces of the nanoparticles is higher than in the bulk [27], and others have suggested that long polymer chains can wrap around several particles, forming a “bridge network” where the particles function as physical cross-links [54]. The evidence in support of such mechanisms has been indirect, or has been extracted from simulations of unentangled chain molecules.

In this thesis results are presented of a systematic study of a model polymer matrix reinforced by a nanoparticle. The nanoparticle is modeled with atomistic detail which allows us to determine the dynamical and mechanical properties as well as glass transition temperature of the bulk reinforcing phase to make connections with micromechanical modeling. The nanoparticles that interact via vdw interactions with the chains are incorporated and the effect of interaction strength is varied. Furthermore, the effect of the size of the nanoparticle as well as chain length is studied. We note that the majority of the systems studied here are below the entanglement limit of the polymers.

1.3. General Approach

The systems of interest in the present study are proteins, polymeric melts pure as well as having embedded nanoparticles. Our interest in proteins stems from our experience in coarse-graining these self-organized natural molecular structures. Since we wish to extend this knowledge to synthetic systems, we study the general properties of oligomers/polymers. Finally, we will combine the knowledge-base obtained in these to predict the properties of synthetic structures that incorporate spherical nanoparticles of various size and interaction strength.

For each system, we will first construct the structure in the way suitable to the simulation technique that will be used: MD or ANM. We will then compare the radial distribution function (RDF) profiles obtained by each approach. We will then extract macroscopic properties of interest.

1.3.1. System structure construction

For each system different structure construction will be applied. For proteins, the coordinates of the backbone geometry will be obtained from the x-ray data that is available in Protein Data Bank (PDB) [69]. In the case of polymers, the equilibrated coordinates obtained from MD simulations will be used following an appropriate amorphous cell construction procedure (in Materials Studio Program) [70]. To construct systems and to check the consistency of their general properties the following steps will be followed:

- a. Construction of amorphous system with polymers/oligomers of different molecular weight (MW), type, temperature, and other environmental conditions of interest.
- b. Obtaining pair correlation function, $g(r)$
- c. Obtaining thermodynamical properties such as characteristic ratio or atomic fluctuations to compare with known experimental values.

1.3.2. Network construction and related microscopic properties

The steps followed in network construction are as follows:

- a. Obtaining appropriate cutoff distance that provides the same neighborhood information as the RDF.
- b. Applying ANM to the equilibrated backbone geometry of the system that is obtained from the constructed network .
- c. Obtaining dynamical and static physical properties such as B-factors, vibrational frequency distribution, total energy and partition function of the network.

1.3.3. Extraction of Properties

We calculate the following properties to gain an overall understanding of the microscopic effect of local heterogeneities to observables:

- a. Macroscopically measurable thermal, mechanical and structural properties such as heat capacity, isothermal compressibility (κ_T), elastic modulus, intrinsic viscosity (η), glass transition temperature (T_g), radius of gyration (R_g) etc.
- b. Kinetic properties such as diffusion coefficient on the macroscopic scale, and various relaxation times of chain units on the microscopic scale.

This protocol is applied for different sets of input parameters such as T , density, polymer type and length (MW), in order to obtain output macroscopic (material) properties and how they are related to these input parameters.

2. THEORETICAL BACKGROUND AND METHODS

2.1. Theory

2.1.1. Radial and angular distribution functions

The radial distribution function (RDF), $g(r)$, is a measure of the correlation between the locations of particles within a system, measured as the probability of finding another particle at a distance, r , from a chosen particle, normalized by the volume element and computed through the relation:

$$g(\vec{r}) = \frac{1}{N} \sum_{i=1}^N \sum_{j=1}^N \delta(\vec{r} - (\vec{R}_j - \vec{R}_i)) \quad \text{for } \vec{r}_{ij} = \vec{R}_j - \vec{R}_i \quad (2.1)$$

where N is the number of particles, R_j is the position vector of j th particle and δ is Kronecker delta function.

The RDF is a useful tool to describe the structure of a molecular system, particularly those of liquids. In an ordered solid, RDF has an infinite number of sharp peaks whose separations and heights are characteristic of the lattice structure. RDF can be deduced experimentally from X-ray or neutron diffraction studies, thus providing a direct comparison between experiment and simulation.

We are not only interested in the number distribution of particles around a given node, but also concentrate on the link structure. We treat all neighbors of a node equivalently, and we find that as r_c is increased with the addition of new neighbors to each node, the resultant vector, Q_i , on node i due to all its neighbors, j , converges to a certain location:

$$Q_i = \sum_j A_{ij} \mathbf{R}_{ij} \quad (2.2)$$

where \mathbf{R}_{ij} is the unit vector connecting residue pairs i and j , and A_{ij} are the elements of

the adjacency matrix. An example is shown on a 54 residue α -helical protein (PDB code: 1enh) in figure 2.1, where the length of a red vector is proportional to r_c and demonstrate that at small r_c , the neighbors of a node are at distinct locations, whereas with increasing r_c , the new nodes are added in a spherically symmetrical manner so that the resultant vector, \mathbf{Q}_i , is only slightly modified. The resultant vectors from the Voronoi tessalated network structure is also shown (in yellow) and is found to be different from the converged ones.

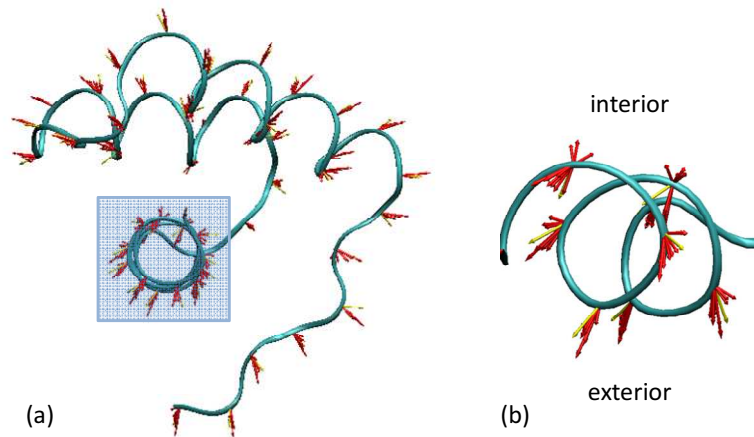


Figure 2.1. (a) The negative of the resultant vectors acting on the nodes, $-\mathbf{Q}_i$, exemplified by a 54 residue protein (PDB code: 1enh). The length of each red vector is proportional to the cut-off distance used in network construction, r_c , the shortest at 7 Å and the longest at 15 Å. The yellow vector is the resultant obtained from the networks obtained from the Voronoi tessalations. (b) Part of the helix marked by the square in (a) is magnified; “exterior” refers to the solvent contacting part of the helix, and “interior” marks the side facing the core of the protein.

To quantify this behavior, we define the angular distribution function (ADF), which is the distribution of angular change, $\Delta\phi$, of the resultant vector obtained from the contacting residues at a distance r to $r+dr$ to the reference residue:

$$\cos \Delta\phi_i(r) = (\sum_j A_{ij} \mathbf{R}_{ij})_r \cdot (\sum_j A_{ij} \mathbf{R}_{ij})_{r+dr} = \mathbf{Q}_i|_r \cdot \mathbf{Q}_i|_{r+dr} \quad (2.3)$$

where dr is a small perturbation on the distance r .

2.1.2. From $g(r)$ to thermodynamic relations

Importance of the radial distribution function comes from the fact that when the total potential energy of the N -body is assumed to be pair-wise additive, *i.e.*

$$U_N(\vec{r}_1, \dots, \vec{r}_N) = \sum_{i < j} u(r_{ij}) \quad (2.4)$$

where the summation runs over all pairs of particles in the system, then all the thermodynamic functions of the system can be related to $g(r)$ [71].

In order to calculate all thermodynamic properties, one has to have three equations of state. In terms of $g(r)$, the most convenient triplet is that of energy, pressure and chemical potential.

The total energy is the sum of mean kinetic and mean potential energy:

$$\frac{E}{Nk_B T} = \frac{3}{2} + \frac{\rho}{2k_B T} \int_0^{\infty} u(r) g(r, \rho, T) 4\pi r^2 dr \quad (2.5)$$

where ρ is the density (N/V) and k_B is the Boltzmann constant. The pressure is related to $g(r)$ through:

$$\frac{p}{k_B T} = \rho - \frac{\rho^2}{6k_B T} \int_0^{\infty} r u'(r) g(r) 4\pi r^2 dr \quad (2.6)$$

The last thermodynamic property, which is non-mechanical, is the chemical potential. Introducing a coupling parameter ξ , which ranges from 0 to 1, to replace the interaction of the central molecule (1) with the j^{th} molecule of the system, total potential energy may be modified to:

$$U(\vec{r}_1, \dots, \vec{r}_N, \xi) = \sum_{j=2}^N \xi u(r_{1j}) + \sum_{2 \leq i < j \leq N} u(r_{ij}) \quad (2.7)$$

The chemical potential finally will have the form:

$$\frac{\mu}{k_B T} = \ln \rho \Lambda^3 + \frac{\rho}{k_B T} \int_0^1 \int_0^\infty u(r) g(r; \xi) 4\pi r^2 dr d\xi \quad (2.8)$$

where Λ is a constant called the thermal *de Broglie* wavelength, defined as $(h^2/2\pi m k_B T)^{1/2}$. Once these three equations of state are known, one can in principle obtain any thermodynamical property of interest through the relevant relationship.

Thus, in order to compute any thermodynamic property from a knowledge of the molecular distribution functions, one needs to know the potential at a given point as a function of distance, $u(r)$ and the coupling parameter ξ . For mechanical properties, such as the heat capacity or coefficient of thermal expansion, the latter is not necessary.

2.1.3. Prediction of the effective intermolecular potential $u(r)$

When we take the logarithm and then take the gradient with respect to the position of one of the n molecules of both sides of the definition of correlation function, $g^n(r_1, \dots, r_N)$ [71]:

$$\nabla_j \ln g^n(r_1, \dots, r_N) = \frac{\int \dots \int e^{-\beta U} (-\nabla_j U) dr_{n+1} \dots dr_N}{\int \dots \int e^{-\beta U} dr_{n+1} \dots dr_N} \quad j = 1, 2, \dots, n \quad (2.9)$$

where n is the number of particles in the interaction (n -body) and $-\nabla_j U$ is the force acting on molecule j due to molecules fixed at position r_1, \dots, r_N .

So the right hand side of the equation gives the mean force acting on j averaged over the configurations of other particles. We will focus on $g^2(r_1, r_2)$, since it may be experimentally determined from x-ray or neutron diffraction and we can have this information directly from the pair correlation function $g(r)$. The integration of this mean

force over all other $N-2$ particles approximates the intermolecular potential, $u(r)$, when the density of the system is sufficiently low.

$$\int \nabla \ln g^2(r_1, r_2) = \ln g^2(r_1, r_2) = u(r_1, r_2) = u(r) \quad (2.10)$$

where r is relative distance between the particles (1) and (2).

2.1.4. Anisotropic network model as a coarse-grained method

In ANM that was originally developed for proteins, each node is represented by the α -carbon coordinates of the residues in a folded protein, and the interactions between them are considered to be due to harmonic potentials. Nodes within the predetermined cutoff distance r_c are coupled by elastic springs having a uniform force constant γ . Thus the overall potential of the molecule is given by the sum of all harmonic potentials among interacting nodes such that

$$V = \frac{\gamma}{2} \sum_i \sum_{j>i} (A_{ij})(R_{ij} - R_{ij}^0)^2. \quad (2.11)$$

Here A_{ij} is the ij th element of the Kirchhoff matrix Γ of inter-residue contacts. This term is equal to 1 if the distance between nodes i and j , R_{ij} , is smaller than the cutoff distance r_c , zero otherwise. R_{ij}^0 is the equilibrium distance between corresponding residues. For a network of N nodes, the Hessian matrix is a $3N \times 3N$ matrix formed by a number of N^2 super elements H_{ij} . The off-diagonal super elements of H_{ij} ($i \neq j$), obtained from the second derivative of the total potential with respect to node positions, are given by

$$H_{ij} = \frac{\gamma A_{ij}}{(R_{ij}^0)^2} \begin{bmatrix} X_{ij} X_{ij} & X_{ij} X_{ij} & X_{ij} Z_{ij} \\ Y_{ij} X_{ij} & Y_{ij} Y_{ij} & Y_{ij} Z_{ij} \\ Z_{ij} X_{ij} & Z_{ij} Y_{ij} & Z_{ij} Z_{ij} \end{bmatrix} \quad (2.12)$$

where X_{ij} , Y_{ij} , and Z_{ij} are the Cartesian components of the distance vector R_{ij}^o . The pseudo-inverse of H is the $3N \times 3N$ covariance matrix, C , that can be expressed in terms of the $3N-6$ non-zero eigenvalues λ_k and corresponding eigenvectors \mathbf{u}_k of H as:

$$C = \sum_{k=1}^{3N-6} \frac{1}{\lambda_k} \mathbf{u}_k \mathbf{u}_k^T \quad (2.13)$$

Here, the eigenvectors \mathbf{u}_k represent the spatial dependence (direction) of each mode λ_k . The smallest nonzero eigenvalue λ_0 corresponding to the lowest frequency is assumed to carry information on the most collective internal modes of motion. The residue fluctuations are predicted by the ANM for residue i from the trace of C_{ii} . Theoretically, they are related to the B-factors determined from x-ray crystallographic data through the relation,

$$\mathbf{B}_i = (8\pi^2 k_B T / 3\gamma) \text{tr}(\mathbf{C}_{ii}) \quad (2.14)$$

where k_B is the Boltzmann constant and T is the absolute temperature. The value of γ is determined *a posteriori* if experimental data are available, and does not affect the fluctuation profile of residues.

2.2. Methods and Systems Studied

2.2.1. Molecular dynamics (MD) simulation

Molecular dynamics is the integration of classical Newton equations to generate successive configurations of the system in time [5]. Trajectory of particles, defined by their positions and velocities, may be obtained from the Newton's second law:

$$m_i \ddot{r}_i = f_i \quad (2.15)$$

where f_i , m_i , and r_i are force exerted on, mass and position of particle i , respectively. The force is the gradient of potential on particle i , which is defined as the sum over all the effective interactions of all other particles with i :

$$f_i = -\frac{\partial U(r_1 \dots r_N)}{\partial r_i} \quad (2.16)$$

The solution of equation 2.16 reproduces a trajectory of atomic coordinates and velocities. In principal using this information, one may compute any property of interest, for example the total mean energy by adding the kinetic and potential energies of each particle's position and velocity, averaging over consecutive time intervals,

$$\langle E \rangle = \frac{1}{t} \sum_t E_t \quad (2.17)$$

Heat capacity may then be obtained by the relation:

$$C_v = \frac{\langle E^2 \rangle - \langle E \rangle^2}{k_B T^2} \quad (2.18)$$

In practice, one is limited by computational power. Since the molecular potentials have complex forms, there is no analytical solution of the equations of motions. Numerical methods and algorithms are used to obtain the trajectories of particles. The potential energy, U , can be separated into non-bonded and bonded interactions:

$$U(r_1 \dots r_N) = U_{bonded}(r_1 \dots r_N) + U_{non-bonded}(r_1 \dots r_N) \quad (2.19)$$

Non-bonded potential is composed of 1-body, 2-body and higher body terms,

$$U_{non-bonded}(r_1 \dots r_N) = \sum_i v(r_i) + \sum_i \sum_{j>i} u(r_i, r_j) + .. \quad (2.20)$$

however, for simplicity higher order terms are neglected and the pair potential is used. The $v(r)$ term represents the applied external potential, and the two body interaction potential, $u(r_i, r_j)$ equals to $u(r_{ij})$. There are numerous experimental and theoretical

models on how to define these potentials, Lenard-Jones potential being the most commonly used:

$$u_{LJ}(r) = \frac{a}{r^6} - \frac{b}{r^{12}} \quad (2.21)$$

In the presence of charges, a Columbic interaction is also added. For simplest intramolecular interaction potential, vibrational harmonic form can be used by including summation over all bonds and bond bending angles in addition to a periodic function of torsional angles:

$$u_{\text{int ra}} = \frac{1}{2} \sum_{\text{bonds}} k_{ij}^r (r_{ij} - r_{eq})^2 + \frac{1}{2} \sum_{\text{bond angles}} k_{ijk}^\theta (\theta_{ijk} - \theta_{eq})^2 + \frac{1}{2} \sum_{\text{torsional angles}} \sum_m k_{ijkl}^{\phi,m} (1 + \cos(m\phi_{ijkl} - \gamma)) \quad (2.22)$$

where k_r , k_θ , and k_ϕ are constants that depend on the identity of the atoms participating in the interaction, r_{eq} and θ_{eq} are the average bond length and angle, m and γ depend on the rotameric states of the torsional angle.

A reliable simulation force-field package has the specification of the strength parameters and constants and/or other additional terms those have been obtained by matching experimental and/or quantum mechanical data, and have been tested for a wide variety of systems.

Using these potentials and current computers, one may simulate systems of 10^5 particles up to time scales of sub-microseconds. In simulations of oligomer/polymer systems, different techniques that utilize coarse-graining of the system have been developed to predict properties of much larger systems at long time scales that are currently not accessible through MD.

2.2.2. Molecular modeling and simulation details for PBD melts

Monodisperse 32 chain *cis*-1,4-polybutadiene melt system with 32 repeating units (C_{128}) was used in all of the simulations, unless otherwise specified. To see the

thermal and pressure effects, different temperatures and pressures (see table 2.1) were carried out under isothermal-isobaric (NPT) conditions.

Table 2.1. Summary of MD Simulations at the data collection stage

Pressure (atm)	Temperature (K)	Sim. Time (ns)
1	300, 340, 380, 410, 430	55,15,15,15,15
1000	300, 340, 380, 410, 430	15
2000	380	15
3000	380	30

United-atom model was employed according to the work of Gee and Boyd [72]. With little sacrifice in accuracy, united-atom model provides a higher computational efficiency when compared to other all-atom force fields. Each CH_n group in the chain is represented as an interacting node (see figure 2.2). The force field-parametrization details of the model are listed in table 2.2.

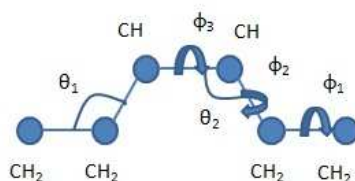


Figure 2.2. United-atom model representation of *cis*-1,4-PB

In order to have physically and thermodynamically realistic systems, the procedure below was applied prior to the data collection stage:

1. Amorphous cell construction of *cis*-1,4-polybutadiene with Materials Studio 4.4 suite of programs [73] (density was chosen to match the experimental value of 0.92 gr/cm^3)
2. Minimization at 300 K with NAMD Program [74] (10 ps)
3. NPT simulation at extremely low density (approximate 47 \AA cubic sized chains immersed into 300 \AA length box) and 300 K (50 ps)
4. NPT simulation at 10^6 atm at 300 K in order to reduce the characteristic ratio of the chains, C_n , to match experimental values (150 ps)

5. NPT simulation at 1 atm and 430 K in order to relax the system (1 ns)
6. Data collection stage with NPT simulation at different temperatures and different pressures as indicated in table 2.1.

For all simulations, 1 fs integration time step was used. Temperature and pressure of the system were maintained constant in the MD simulations at their prescribed values by employing the Langevin thermostat-barostat. For the non-bonding interaction cut-off distance of 10 Å was used with switching distance of 8 Å.

Table 2.2. Force-field parameter of united-atom model used for MD simulations [75]

Interaction	Potential Form	Parameters									
Bond Stretching	$V_{str} = \frac{1}{2}k_{str}(l-l_0)^2$	Type	$k_{str}(\text{kcal/mol. } \text{Å}^2)$					$l_0(\text{Å})$			
			1	158.5					1.54		
			2	183.8					1.5		
			3	246.9					1.34		
Bending	$V_{\theta} = \frac{1}{2}k_{\theta}(\theta-\theta_0)^2$	Type	$k_{\theta}(\text{kcal/mol. rad}^2)$					Θ (deg.)			
			1	115					111.65		
			2	89.4					125.89		
Torsion	$U(\phi) = \frac{1}{2} \sum_{n=1}^6 k_n(1-\cos(n\phi))$	Type	k_1	$k_2(\text{kcal/mol})$		k_3	k_4	k_5	k_6		
			3	-	24.2		-	-	-	-	
			2	1.033	-0.472		0.554	0.263	0.346	0.164	
			1	-0.888	-0.619		-3.639	-0.666	-0.247	-0.190	
Nonbond	$V_{ij} = 4e \left[\left(\frac{\sigma}{r_{ij}} \right)^{12} - \left(\frac{\sigma}{r_{ij}} \right)^6 \right]$	Type	ϵ (kcal/mol)					$r_{\min}(\text{Å})$			
			1	0.0936					4.5		
			2	0.1					3.8		
			3	0.1015					4.257		

2.2.3. Network construction from PBD melt simulations

A polymer of N monomers is treated as a residue-based structure, where the -CH atom of each repeating butadiene unit is considered as a node, of which the coordinates are obtained from fully relaxed constant pressure MD simulations. The network information is contained in the $N \times N$ adjacency matrix, A , of inter-residue contacts, whose elements A_{ij} are taken to be one (1) for contacting pairs of nodes i and j , and zero (0) otherwise. We establish a link between two nodes if they are within a cut-off distance r_c of each other.

For cut-off selection, we chose different cut-off values ($r_{cut} = 5, 7.5, 10$ and 12.5 Å) and calculated the correlation of the RMS-fluctuation obtained from ANM with the RMS-fluctuation from MD simulation. Correlation of RMS-fluctuation of ANM and MD at $r_{cut} = 5$ Å is close to zero and reaches to a plateau (approx. 0.5) at $r_{cut} = 7.5$ Å and for higher cut-off values correlation does not improve, displaying very similar RMS-fluctuation patterns as depicted in the figure 2.3. Since, higher cut-off values do not improve correlation, cut-off value of 7.5 Å was chosen for network construction in order to decrease the amount of processing time.

RMS-fluctuation is obtained from ANM by obtaining the trace of C_{ii} as explained in the section 2.1.4. ANM is applied to 15 consecutive time frames each separated by 1 ns and the averages are reported. The RMS-fluctuations obtained from the MD simulation were calculated directly from the MD trajectory. After computing the average x, y, z coordinates of the selected atoms, the RMS distance of each atom from that position were computed for 1500 time frames of 10 ps intervals. In the calculations of the RMS-fluctuations both from the ANM and MD were applied periodic boundary conditions (PBC). The procedure for the PBC correction is explained in Appendix A.

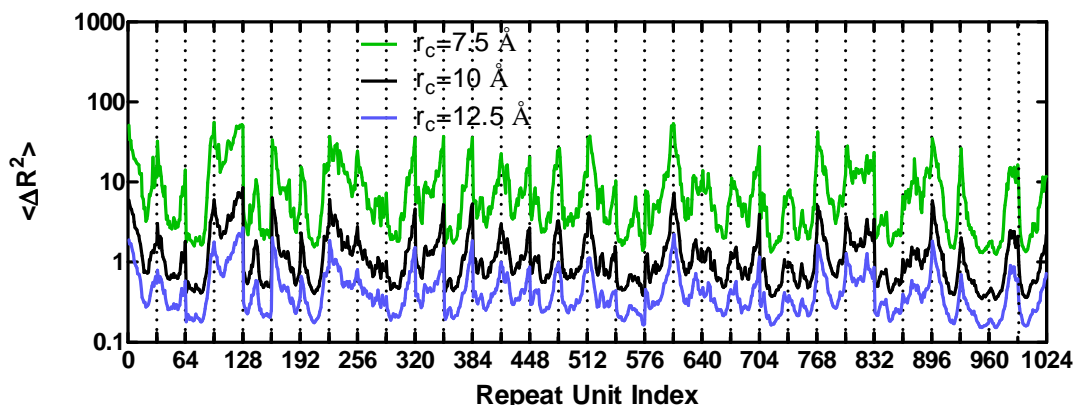


Figure 2.3. RMS-fluctuations obtained from ANM for different cut-off values ($r_{cut}=7.5$ Å, 10 Å and 12.5 Å).

2.2.4. Simulation details for PBD melts with nanoprobes

Nanoclusters having radii ranging from 3.16 Å to 7.12 Å (number of atoms from 10 to 150) are embedded in the *cis*-1,4-polybutadiene (32 chains each with 32 repeating units of the butadiene monomer) in order to obtain the diffusion coefficient and predict the zero-shear viscosity of the polymer as well as to understand nanoclusters' behavior and influence on the polymer's thermodynamic properties. The nanoclusters with 10, 40 and 150 atoms are depicted in the figure 2.4. As the number of the atoms increases, the nanoclusters obtain to more spherically-symmetric form.

In this study, seven set of cluster size ($N = 10, 20, 30, 40, 70, 100$ and 150) for four temperature sets (at 280, 330, 380 and 430 K) were conducted (table 2.3). Since *cis*-1,4-polybutadiene of molecular weight (MW) 55000 g/cm³ has a T_g approximately at 170 K [76], the simulation temperatures were chosen well above 170 K.

Table 2.3. Overview of the simulations for 32 PBD chains of 32 repeat units

Temperature (K)	Ensemble	Simulation Time(ns)	Nanoclusters Size
280	npt	60	0,10,20,30,40,70,100,150
330	npt	40	0,10,20,30,40,70,100,150
380	npt	20	0,10,20,30,40,70,100,150
430	npt	20	0,10,20,30,40,70,100,150

The fundamental properties of the atoms constituting the nanocluster are taken to be similar to that of silicon. Thus, the atomic mass of the atoms are 32 g/mol, and the well depth for non-bonded interactions between pairs of atoms occurs at 0.854 kcal/mol. The van der Waals radius is taken to be 4 Å. The particle coordinates of the nanocluster are obtained from the Cambridge Cluster Database [77] and those pairs that are within 2.23 Å of each other are connected by springs with spring constant $k = 150$ kcal/mol. These particles otherwise interact with each other and the rest of the polymeric chains via vdw forces depicted by the Lennard Jones potential. Nanoparticle atom - polymeric chain atom interactions are obtained via geometric mean for the well-depth, and arithmetic mean for the vdw radii, unless otherwise specified. In all simulations, cutoff distance on non-bonded interactions are 10 Å, which are smoothed with a switching function set on at 8 Å. Time step is 2 fs and data are recorded at intervals of 1000 steps (2 ps).

One nanocluster was embedded into the polymer matrix and this polymer-nanocluster composite was equilibrated for 2 ns under 1 atm pressure. This procedure was repeated for nanoclusters with sizes from 10 to 70 atoms. For the nanoclusters with more than 70 atoms, since they cannot be embedded directly into the polymer matrix, the nanocluster is first located on the edge of the polymer box. The resulting larger periodic box was simulated for 1 ns under 1000 atm pressure until a homogenous mixture was obtained and further equilibrated under 1 atm pressure to reach room temperature density.



Figure 2.4. Atomic configurations of the nanoclusters of different sizes ($N=10, 40, 150$)

2.2.5. Network construction from proteins and protein data sets

A protein of N residues is treated as a residue-based structure, where the C_α atom of each amino acid is considered as a node, and the coordinates of the protein are obtained from the protein data bank (PDB) [69]. The network information is contained in the $N \times N$ adjacency matrix, A , of inter-residue contacts, whose elements A_{ij} are taken to be 1 for contacting pairs of nodes i and j , and zero otherwise. We determine the presence of a contact using two approaches, one involving a selected cut-off distance, and the other using Voronoi tessellations. In the former approach, the criterion for contact is that the two nodes are within a cut-off distance r_c of each other. In the latter, Voronoi cells are formed from the PDB coordinates of C_α atoms such that the three dimensional space is uniquely and completely subdivided into polyhedra whose surfaces are defined by the intersection of contact planes built midway between the nodes of the network. Thus, pairs of nodes sharing a common plane are taken to be in contact. This methodology allows eliminating the choice of a cut-off distance so that an unambiguous network construction is achieved [17, 78]. We have utilized the freely available Voro3D program for this purpose [43]. Note that the nodes in these networks have an average distance of 6.6 Å to their neighbors, and an average contact number of 10.5.

We base our calculations on a set of 595 proteins with sequence homology less than 25% and sizes spanning 54–1021 residues [79]. This protein set is identical to that used in previous statistical analyses on residue network published by Atilgan et al. [19, 80]. Forty-five of the proteins in the set have fewer than 100 residues, the number of proteins in the ranges (101–200), (201–300), (301–400), and more than 400 residues are 234, 122, 108, and 86, respectively. A list of all the proteins used, their sizes, and distributions appear in the Supplementary Material of reference [80].

In addition, we have studied the location dependence of certain properties. For this reason, we calculate residue depth from the surface of the protein [81, 82]. We classify residues that are deeper than 4 Å as core, and the rest of them as surface residues. The choice of this value is based on the fact that the size of spatial fluctuations, as calculated from MD simulations on BPTI, of the surface and interior residues converge to the same value at the protein dynamical transition [83]. For the

distinction of core/surface residues, we use a subset of the original protein data set that has a total of 60 representatives with sizes in the range 140 – 320 amino acids. Finally, we also study the eigenvalue spectra of proteins (λ_k in equation 2.13), which is affected by the size of the systems. We therefore choose the subset of 26 proteins for which $N = 150 \pm 10$.

2.2.6. Viscosity measurement experiments

The experimental results are obtained by Bohlin CVO Rotational Viscosimeter at 10 Hz and a strain value of 1 with a similar molecular weight polybutadiene having a %60 *trans*, %20 *vinyl*, %20 *cis* microstructure.

2.3. Properties Calculated

2.3.1. Diffusion coefficient and zero-shear viscosity calculations

The nanoclusters in the polymer melt experience two kinds of forces: Brownian random force and frictional force. So the equation of motion is defined as;

$$m \frac{dv(t)}{dt} = f_B(t) - \gamma v(t) \quad (2.23)$$

Mean Square Displacement (MSD) is calculated by taking ensemble average on 3D coordinates of the nanocluster center all over the simulation time.

$$\langle \Delta r^2(t) \rangle = \langle [x(t + \Delta t) - x(t)]^2 + [y(t + \Delta t) - y(t)]^2 + [z(t + \Delta t) - z(t)]^2 \rangle \quad (2.24)$$

When the log of MSD is plotted against log of time step, Δt , the slope is one for Newtonian fluid obeying the below relation:

$$D = \lim_{t \rightarrow \infty} \frac{\langle [r(t) - r(0)]^2 \rangle}{6t} \quad (2.25)$$

Zero shear viscosity, η_o , may be derived via the Stokes-Einstein equation (below) with using D obtained from MSD:

$$\eta_o = \frac{k_B T}{6\pi a D} \quad (2.26)$$

where k_B is the Boltzmann constant, T , the temperature of the system, a , the radius of nanocluster and D , the diffusion coefficient.

The diffusion coefficients are obtained from the MSD curve where the slope is close to one, satisfying the condition of longer times in equation 2.25. An example of MSD curve of nanocluster with 150 atoms is given in figure 2.5. When D is plotted against $1/a$, the slope of the line fitted to the data points gives the inverse of zero shear viscosity, η_o multiplied by the factor, $k_B T / 6\pi$.

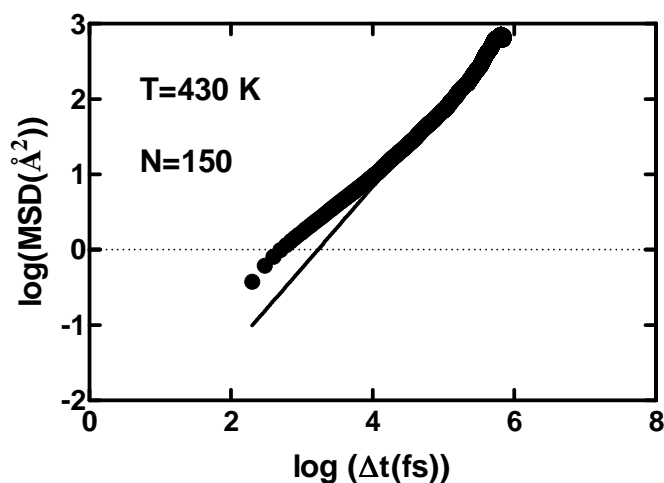


Figure 2.5. Mean square displacements vs. time for diffusion coefficient calculation

2.3.2. Dynamical properties

Time correlations (τ_c) from the ^{13}C -NMR experiments are calculated from the time decay of the second orientational autocorrelation function (OACF), $M_2(t)$, of the butadiene C-H bond vectors via:

$$M_2(t) = \frac{1}{2} [3 \langle \cos^2 \theta(t) \rangle - 1] \quad (2.27)$$

where $\theta(t)$ is the angle between two orientations of the C-H bond at times 0 and t . τ_c is obtained from the integral of the OACF as [84]:

$$\tau_c = \int \frac{M_2(t) - M_2(\infty)}{M_2(0) - M_2(\infty)} dt \quad (2.28)$$

Time correlations from the simulation are extracted by fitting best exponential decay lines to $M_2(t)$:

$$M_2(t) = \frac{1}{2} \left[3 \left(\frac{\langle m(0).m(t) \rangle}{\langle m(0).m(0) \rangle} \right) - 1 \right] \quad (2.29)$$

where $m(t)$ is the bond orientation vector of the butadiene C-H bond.

Another dynamical property of interest is the residence (or escape) time (τ_r) [85] which is an average time of a atom/molecule to escape from a given region. It is used to obtain information on the dynamical behavior of polymer chains that are close to the surface of the nanocluster. We have calculated τ_r by monitoring the number of atoms residing at a distance of one vdw radius. A simple exponential decay function is fitted to the curve of number of residing atoms left with respect to simulation time step:

$$N_r = \langle N_r \rangle \exp(-t/\tau_r) \quad (2.30)$$

where N_r is the number of particles left at the indicated region.

2.3.3. Mechanical properties

The mechanical properties of materials are of great importance in engineering applications. When a mechanical force is applied to a specimen, the deformation of the specimen is described in terms of its *stress-strain* behavior. In an atomistic calculation, the internal stress tensor can be obtained using the so-called virial expression:

$$\sigma = -\frac{1}{V_0} [(\sum_{i=1}^N m_i (v_i v_i^T)) + (\sum_{i<j} r_{ij} f_{ij}^T)] \quad (2.31)$$

where index i runs over all particles 1 through N ; m_i , v_i and f_i denote the mass, velocity and force acting on particle i ; and V_0 denotes the (undeformed) system volume.

For small deformations, the relationship between the stresses and strains may be expressed in terms of a generalized Hooke's law:

$$\sigma_{lm} = C_{lmnk} \varepsilon_{nk} \quad (2.32)$$

where ε is the strain tensor and C is the stiffness matrix.

The stiffness matrix C is a symmetric 6×6 matrix, and hence a maximum of 21 coefficients are required to describe the stress-strain behavior of an arbitrary material fully. For an isotropic material, the stress-strain behavior may be fully described by specifying only two independent coefficients. The resulting stiffness matrix may be written as:

$$\begin{bmatrix} \lambda + 2\mu & \lambda & 0 & 0 & 0 & 0 \\ \lambda & \lambda + 2\mu & \lambda & 0 & 0 & 0 \\ 0 & \lambda & \lambda + 2\mu & 0 & 0 & 0 \\ 0 & 0 & 0 & \mu & 0 & 0 \\ 0 & 0 & 0 & 0 & \mu & 0 \\ 0 & 0 & 0 & 0 & 0 & \mu \end{bmatrix} \quad (2.33)$$

where λ and μ are referred to as the Lamé coefficients. For the isotropic case, the familiar moduli (Young, Bulk and Shear Modulus, respectively) may be written in terms of the Lamé coefficients as follows:

$$E = \mu \left(\frac{3\lambda + 2\mu}{\lambda + \mu} \right) \quad (2.34)$$

$$K = \lambda + 2/3\mu \quad (2.35)$$

$$G = \mu \quad (2.36)$$

Originating in the work of Theodorou and Suter [86], elastic moduli may be estimated by using a completely static method. After having constructed an energy-minimized series of amorphous structures confined to a periodic cube, each structure is subjected to twelve deformations; three pairs in uniaxial tension/compression and three pairs involving pure shear, followed by a reminimization to restore a state of detailed mechanical equilibrium.

Each of these deformations corresponds to setting one of the components of the strain vector to some small value (for example $\varepsilon = 0.001$), while keeping all other components fixed at zero. The elastic stiffness coefficients may then be obtained by estimating the second derivatives of the deformation energy with respect to strain using a finite difference formula (for the diagonal components only), and by calculating $\Delta\sigma_i/\Delta\varepsilon_j$ for each of the six pairs of applied strains, where σ_i represent, in vector notation, elements of the stress tensor obtained analytically using the virial equation. Although this methods gave good agreement for the diagonal elements C_{ii} of the stiffness matrix for the glassy polypropylene samples studied in the Theodorou and Suter's original work, generally it should be assumed that numerical estimation of second derivatives (of the energy) will be less precise than estimation of the first derivatives (of the stress) [87]. In this work we use the implementation of the work of Theodorou and Suter by the Materials Studio Program for all shear modulus calculations.

The bulk modulus $K > 0$ can also be formally defined by the equation:

$$K = -V \frac{\partial p}{\partial V} \quad (2.37)$$

where P is pressure, V is volume, and $\partial P/\partial V$ denotes the partial derivative of pressure with respect to volume. The inverse of the bulk modulus gives a substance's isothermal compressibility. It is more precise to calculate the bulk modulus from the fluctuations of the periodic box volume using simulations at constant pressure by the relationship,

$$K = \frac{k_B T \langle V \rangle}{\langle V^2 \rangle - \langle V \rangle^2} \quad (2.38)$$

2.3.4. Glass transition temperature

Thermodynamic transitions are classified as first- or second-order. In a first-order transition there is a transfer of heat between system and surroundings and the system undergoes an abrupt volume change. In a second-order transition, there is no transfer of heat, but the heat capacity does change. The volume changes to accommodate the increased motion of the wiggling chains, but it does not change discontinuously [88]. Illustrative plots of specific volume vs. temperature are shown in figure 2.6 for amorphous and crystalline polymers.

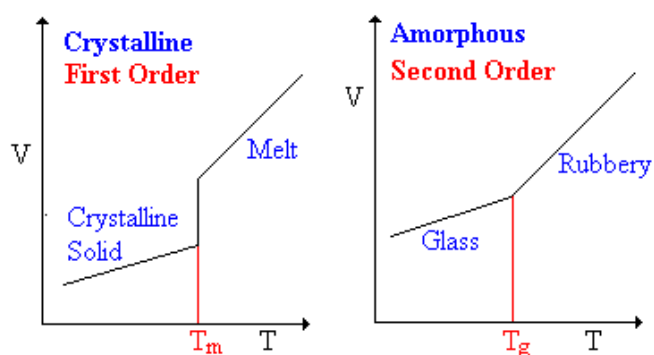


Figure 2.6. Graphical schema of volume-temperature curves for crystalline and amorphous polymer (reproduced from [88]).

When an amorphous polymer is heated, the temperature at which it changes from a glass to the rubbery form is called the glass transition temperature, T_g . A given polymer sample does not have a unique value of T_g , because the glass phase is not at equilibrium. The measured value of T_g will depend on the molecular weight of the polymer, on its thermal history and age, on the measurement method, and on the rate of heating or cooling [89]. In this thesis we calculate the approximate value of T_g from the intersection of the fitted curve to the two different (phase/slope) curves of specific volume vs. temperature data.

3. RESIDUE NETWORK CONSTRUCTION AND PREDICTIONS OF ELASTIC NETWORK MODEL

3.1. Structural Heterogeneity of Amino acid Distributions in Proteins.

The RDF, $g(r)$, of the residues is presented in figure 3.1a for distances up to 20 Å, recorded at 0.1 Å resolution. We find that the first sharp peak in $g(r)$ ends at ca. 6.7 Å corresponding to the first coordination shell (i.e., the range within which residue pairs are found with the highest probability), the second coordination shell occurs at 8.5 Å. Broader peaks ending at 10.5 and 12 Å are identified as the third and fourth coordination shells. At larger distances, $g(r)$ monotonically decreases, indicating that the coarse-grained residue beads do not experience further ordering in the liquid-like environment. In figure 3.1a we also display the ADF, $g(\varphi)$, for the same set of proteins in the same distance range. We find that the main peaks of ADF and RDF overlap, the only difference in the general character of the two distribution functions being found in the third and fourth coordination shells. In RDF, we find that a similar number of particles per unit volume exist in these two coordination shells (same height in the distribution). The ADF provides the additional information that, due to the asymmetry in the intensities of the third and fourth coordination shells, these particles are clustered in relatively more ordered directions in the third shell, quantified by the increase in ADF to ca. 5°. The ADF provides the valuable information that the additional particles are taken into account as more concentric spherical shells of 0.1 Å diameter are added (recall figure 2.1), have a preferred direction of clustering at the regions of higher number density. Conversely, at larger distances, the new neighbors carry directionality that cancel each other out, as would be expected from a random packing of spheres, quantified by the monotonical decrease in $g(\varphi)$.

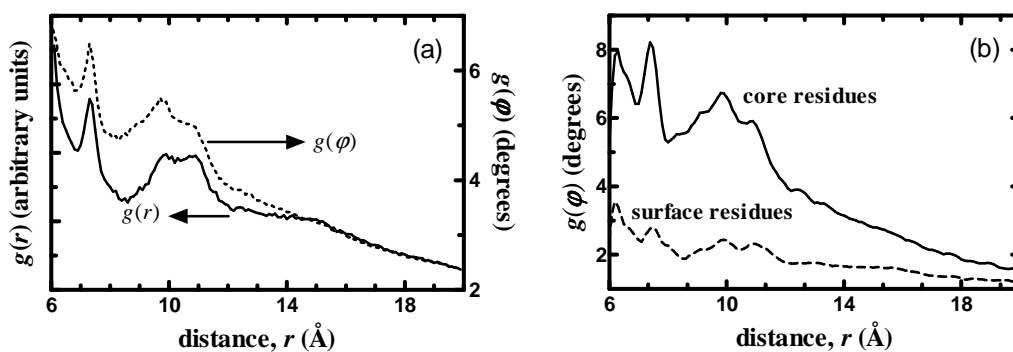


Figure 3.1. (a) Radial and angular distribution functions (left y-axis: RDF; right y-axis: ADF) obtained by averaging over 595 proteins. (b) ADFs computed separately for the core and surface residues for a subset of 60 proteins.

Since globular proteins may be considered to be made up of a core region surrounded by a molten layer of surface residues [90], it is of interest to distinguish the topological differences between the core and the surface (figure 3.1b). We observe that core residues have larger angular changes in the resultant vector, \mathbf{Q}_i (equation 2.2) compared to the surface residues. Note that the fraction of surface residues is ca. 0.6 for these proteins, being somewhat larger for the smaller sized ones [19]. Thus, the resultant vector on the surface residues rapidly converges to a given directionality specific to each residue at short distances, the additional links at higher distances arriving in directions that cancel out. The overall structural heterogeneity is detected much clearly in the $g(\phi)$ of the core residues. However, the heterogeneity in the first coordination shell is more pronounced over that of the second for the surface residues, possibly due to the loose packing in this region. This effect is reversed in the core. In addition, the structural asymmetry between the third and fourth coordination shells is found to originate from the structure of the core residues. The dissimilar behavior of the core and surface regions is also observed in Figure 2.1b. As r increases, the orientation of the vectors are more scattered in the interior, indicating its isotropic nature; conversely, the orientation of the vectors at the surface rapidly converges.

3.2. Density of Vibrational Normal Modes.

The vibrational normal mode spectra, $g(\omega)$, of proteins was originally studied by ben-Avraham for five proteins with sizes in the range of 39 – 375 residues, the data

collapsing on a single curve, especially in the slow mode region [22, 91]. The density of states was found to increase linearly with the frequency in this region, implying a spectral dimension of $d_s = 2$ and deviating from the Debye model of elastic solids where the expected value is [92]. The anomalous spectral dimensions of proteins was also confirmed by inelastic neutron scattering experimental measurements, which yielded $d_s \approx 1.4$ for hen egg white lysozyme [93]. More recently, an equation of state relating the spectral dimension, fractal dimension and the size of a protein was developed based on the coexistence of stability and flexibility in folded proteins [94].

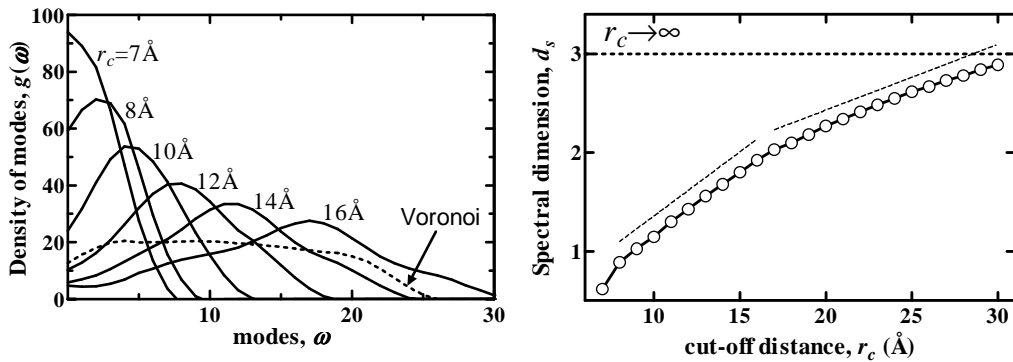


Figure 3.2. (a) The change of the density of vibrational modes, $g(\omega)$, with the cut-off distance, r_c , used in network construction. The main figure displays the results for r_c in the first ($r_c = 7 \text{ \AA}$) to above the fourth coordination shell range (up to 16 \AA). Also shown, in dashed lines, is the frequency distribution of the Voronoi tessalated networks. The inset displays the results for very large r_c values (up to 30 \AA). The data is an average over a set of 26 proteins in the size range of 150 ± 10 residues. (b) Spectral dimension, d_s , of the networks, obtained from power law best-fits to the cumulative density of modes, $G(\omega) \propto \omega^{d_s}$ for the first 70 modes in each set of data. Goodness of fit is 0.98 or better in all cases. The thin dashed lines are included to guide the eye for the cross-over in the rate of change of d_s with r_c . Also indicated on the figure are the d_s of the Voronoi tessalated networks that occur at ca. 1.0, and the theoretical limit at $d_s = 3$ when all nodes are interconnected ($r_c \rightarrow \infty$).

In the original ANM study, the cut-off distance used in network construction was roughly chosen to mimic this distribution of the modes [24], which was 13 \AA for the retinol binding protein studied therein; however, a wide range of cut-off distances appear in the literature based on other criteria, as discussed in the Introduction. Nevertheless, constructing networks with harmonic potentials whose spectra closely

mimic the vibrational modes from all-atom systems seems to be the most plausible approach, since this implies that the curvatures of the energy functions used in the two approaches are adequately approximated, so that the equilibrium properties would be described properly.

In figure 3.2a, we display the r_c dependence of normal mode spectra averaged over 26 proteins of size 150 ± 10 residues, enabling us to disregard the size effect in the calculations [the latter was addressed in references [94] and [95] In general, the low-frequency band of the graph is responsible for large amplitude collective motions related to function, whereas the high-frequency band refers to small amplitude motions of individual residues. We find that at $r_c = 7 \text{ \AA}$ (where neighbors are from the first coordination shell), the distribution is characterized by a direct drop in density with increasing frequency; at this value, most proteins have additional zero eigenvalues, apart from the six due to the rigid body motions. The universal behavior of the slow vibrational modes of proteins is recovered at higher r_c values. Above the cut-off distances that include the fourth coordination shell ($r_c > 12 \text{ \AA}$), a shoulder in the higher frequency region first appears, then broadens as r_c is increased. At $r_c > 16 \text{ \AA}$, a two-peaked density profile that is uncharacteristic of proteins sets in (inset to figure 3.2a). For the networks obtained with Voronoi tessalations (dashed line in figure 3.2a), the distribution shows a flat behavior, also uncharacteristic of proteins. Also note that, although the average distance between adjacent nodes is 6.6 \AA in these systems, their behavior is markedly different from that of the networks with similar cut-offs (e.g. $r_c = 7 \text{ \AA}$.)

Thus, an r_c value in the range of $8 - 16 \text{ \AA}$ captures the general shape of protein vibrational spectra. Yet, inasmuch as one utilizes network models to study collective motions of proteins as a superposition of several low frequency modes, it is important to capture the distribution in the slow mode region of the protein in more detail. This region is intimately related to material properties, characterized by the spectral dimension, d_s . In figure 3.2b, we plot the spectral dimensions of these systems, obtained from power law best-fits to the cumulative density of modes, $G(\omega) \propto \omega^{d_s}$ for the first 70 modes in each set of data [with $dG(\omega)/d\omega = g(\omega)$]. The dimensions approach the Debye model value of 3 as r_c is increased (dotted line in the figure 3.2b). The spectral dimension of the Voronoi tessalated networks is 1.0, and is commensurate with that of

the network at $r_c = 9 \text{ \AA}$. The spectral dimensions in the r_c range from the second to the fourth coordination shell, (8 – 12 \AA increase from below $d_s = 1$ to ca. $d_s = 1.5$). Furthermore, a crossover in the rate of change of the spectral dimension with the cut-off distance occurs at $r_c = 16 \text{ \AA}$, the slope reducing from ca. 0.13 to half this value; the crossover is accompanied by the shift to $d_s > 2$. Thus, it is plausible to use the cut-off value up to 16 \AA so as to capture both the general shape of the vibrational spectra of proteins, as well as the spectral dimension that describes the density of slow modes.

3.3. Biological Significance.

The level of success of the studies in relation to the method of network construction in proteins has not been addressed systematically. We find for a number of proteins that the correlation between the mean-square fluctuations of C_α atoms and the theoretical predictions of equation 2.14 improve as the cut-off distance is increased. This curious observation is valid up to very large r_c values; i.e. for some proteins, even when all residues are interconnected, the fluctuations of individual residues are faithfully predicted. One example is displayed in figure 3.3 for a 263 residue α -class protein (PDB code: 1arb), where the residue-by-residue experimental B-factors (middle curve in gray in figure 3.3a) are compared with several selected theoretical models: A relatively low correlation is obtained at $r_c = 8 \text{ \AA}$; in particular, the fluctuations of surface loop residues 15 – 20 and 135 – 145 are overestimated due to the absence of important core-region contacts that are not taken into account at this cut-off distance. The $r_c = 15 \text{ \AA}$ model captures the experimentally determined fluctuation patterns, which remains unaltered at higher cut-offs. The fluctuations predicted by the Voronoi tessalated network model are somewhat chaotic, lowering the correlations with experiment. The Pearson correlation coefficients at a wide range of cut-off distances are plotted in figure 3.3b, along with the value obtained from Voronoi tessalated networks (dashed line). We emphasize that the behavior exemplified by figure 3.3 is not unique to this protein, but is rather a common property of all proteins.

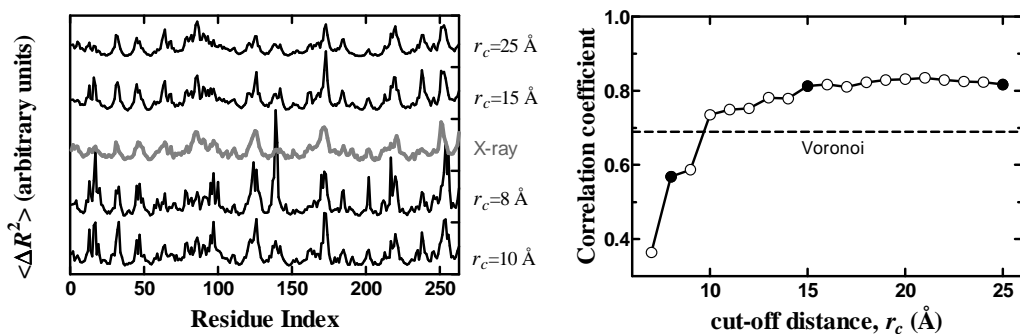


Figure 3.3. (a) Comparison of the X-ray B-factors (gray, middle curve) with fluctuation profiles predicted from various models (at $r_c = 8, 15, 25 \text{ \AA}$ and network construction with Voronoi tessalations) for the 268 residue achromobacter lyticus protease (PDB code: 1arb). (b) Pearson correlation coefficients at a wide range of cut-off distances for the same protein; those that correspond to the detailed fluctuation profiles of figure 3.3a are shown with filled circles and that with the cut-off free Voronoi tessalated model is marked by the dashed line.

In summary, with our analysis over a large set of non-homologous proteins, the degree of success of network models of proteins is shown to converge as the cut-off distance used in constructing the network from the PDB coordinates of the protein is increased. A choice of high r_c in the vicinity of 16 \AA covers the neighborhood structure of an arbitrary protein and its eigenvalue spectra; however, for large proteins, this will introduce a large number of interactions which will render the matrix inversion procedure rather cumbersome. In such cases, one may resort to compute $g(r)$, $g(\varphi)$ and $g(\omega)$ curves and spectral dimensions for the particular protein to choose an optimum r_c ; for large proteins the number of nodes will be high enough to obtain statistics for smooth curves where the peaks may be discerned, a problem that cannot be circumvented for small system sizes. We note that network models are useful in describing the properties related to the fluctuations near the minimum of the conformational energy well, and its curvature. However, they will not succeed in providing information of the dynamical properties of the protein, unless a methodology for updating the Hessian along the reaction coordinate is introduced.

4. PREDICTIONS OF THERMODYNAMIC MEASURABLES OF CIS-1,4-POLYBUTADIENE BY ANM

4.1. Thermodynamical and Structural Properties

The variation of specific volume (v) with T at 1 atm and 1000 atm, as obtained from MD simulations, and depicted in figure 4.1a, indicates that v increases linearly as T is increased for both pressure sets. However, the specific volume values obtained from MD simulation at 300 K is slightly higher than the experimental value of $v=1.086$ cm³/gr. The linearity of the specific volume with increasing temperature is in accordance with the empirical Tait equation which is valid for most of the amorphous polymers [96].

Another important thermodynamic parameter that may be obtained from the simulations is the isothermal compressibility, κ_T ,

$$\kappa_T = \frac{\langle V^2 \rangle - \langle V \rangle^2}{k_B T \langle V \rangle} \quad (4.1)$$

where k_B is the Boltzmann constant and T is the temperature of the system. It is observed that as depicted in the figure 4.1b, κ_T increases in a non-linear form with increasing T at 1 atm, whereas increases very little at 1000 atm (almost independent of temperature for high pressures). The predicted value for κ_T at 300 K is 11.3×10^{-10} Pa⁻¹ and is in agreement with the experimental value (7.2×10^{-10} Pa⁻¹) reported by DiBenedetto for a 1,4 PBD sample of unspecified microstructure at 298 K [97].

Chain conformational properties in the simulated polymer and the effect of temperature and pressure on the overall size of the macromolecular chain may be discussed in terms of characteristic ratio, C_n , calculated from the mean-square chain end-to-end distance, $\langle R^2 \rangle$, through the equation:

$$C_n = \frac{\langle R^2 \rangle}{n \bar{l}^2} \quad (4.2)$$

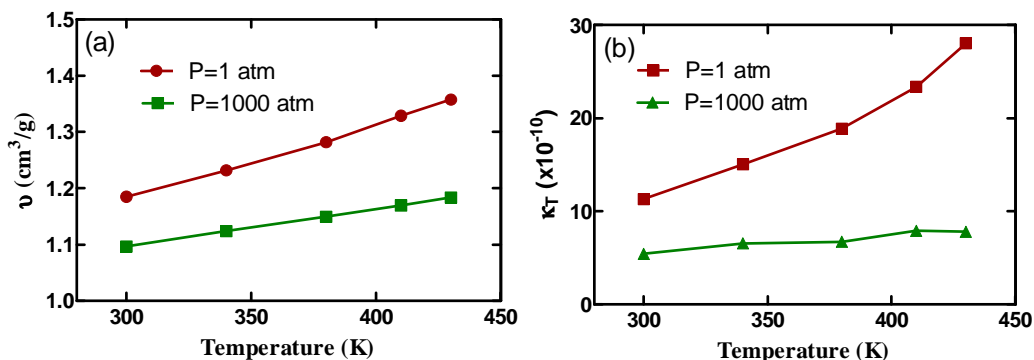


Figure 4.1. (a) Temperature dependence of isothermal compressibility (κ_T) and (b) specific volume (v) at 1 atm obtained from MD simulations.

where n denotes the number of links in the chain backbone and \bar{l}^2 the average squared skeletal bond length. The temperature and pressure effect on C_n for the simulated polymer is presented in figure 4.2. C_n is observed to remain practically constant over the temperature range at 1 atm with a variance of 1.0 - 1.5 Å. This result agrees well with the experimental data of Fetters et al. [98] that the ratio $\langle R^2 \rangle / M$ in 1,4 PBD remains the same in the temperature range 298–413 K. At 1000 atm, C_n remains constant with a much lower standard deviation and increasing slightly as the temperature is increased from 300 to 430 K.

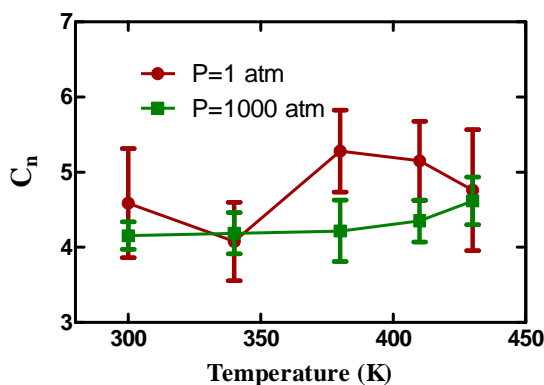


Figure 4.2. Characteristic ratio of the *cis*-1,4-PBD obtained from MD simulations at different temperatures.

The effect of temperature and pressure on the local structure is investigated by using the intermolecular pair distribution function, $g(r)$. Only one of sp^2 atoms of the

butadiene monomer were chosen as the center of nodes for coarse-graining. RDFs were obtained from these nodes and are depicted in figure 4.3.

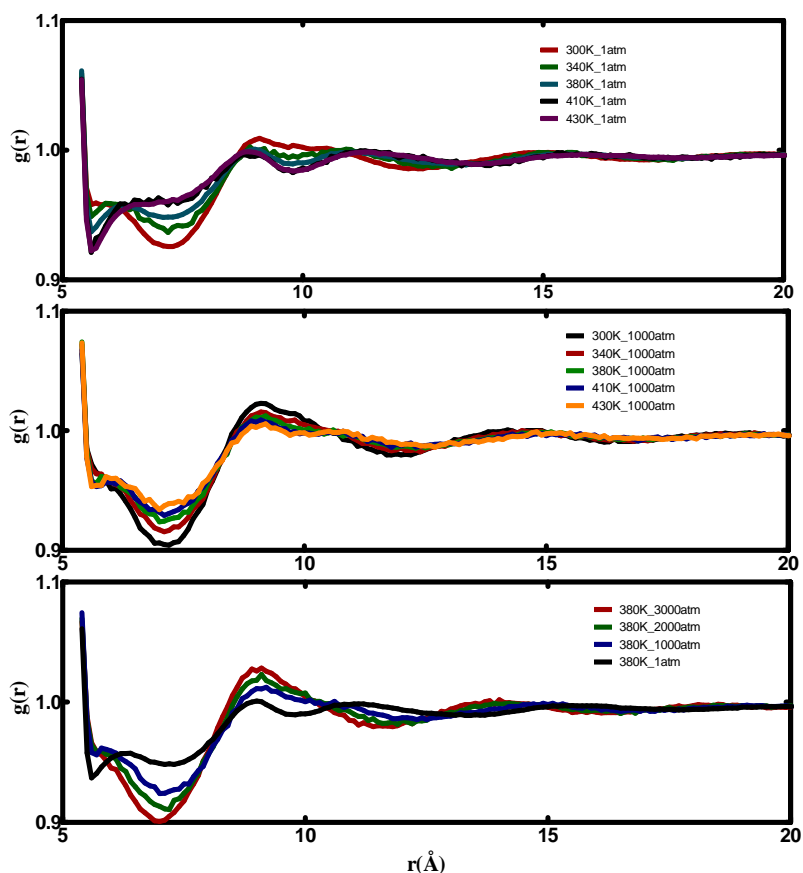


Figure 4.3. Radial distribution function (RDF) of 14 sets of MD simulations

At all pressure and temperature sets, we find that RDF has a sharp peak around 6 Å corresponding to the first coordination shell (one sp^2 with ~ 1.33 Å bond length, three sp^3 with ~ 1.52 Å bond length) between the sp^2 atoms of two butadienes. Two broader peaks, one in the range 6.5 - 8 Å and the other in the range 8 -10 Å constitute the second and third coordination shells, respectively. Because of the rotational freedom of three sp^3 bonds, the tail of the first peak corresponding to first coordination shell has a shoulder vanishing at 4 Å. Moreover, a few broad peaks with very small probabilities beyond 10 Å appear as higher order coordination shells. After approximately 15 Å, all the peaks converge to one, indicating no ordering beyond this distance.

4.2. Thermal Fluctuations

The fluctuations of the polymers and proteins affect their functionality and also give information about the globular and local motions which can be checked with the experimental techniques such as XRD and Nuclear Magnetic Resonance (NMR). Average thermal fluctuations, which are defined as random deviations of a system from its equilibrium, may be calculated by the root mean square displacement (RMSD) (see section 2.1.4).

In figure 4.4, the vector normalized average RMSD values of chains calculated from ANM and MD are compared to see the effect of temperature and pressure on the fluctuations of the chains. Averaging was applied after vector normalizing ($\mathbf{u}\cdot\mathbf{u}^T=1$) each RMSD value of all nodes. The RMSD values from ANM and MD are in good correlation showing similar qualitative behavior such as at the end of the chains increasing 3-4 folds when compared to the center of the chains. This behavior is expected since the ends of the chains are not connected and have higher degrees of freedom with respect to the center of the chains. There are some peaks and irregularities in the fluctuations obtained from ANM and MD data at 3000 atm which also results in lower correlations. Thus, the limit of applicability of ANM to PBD is around 3000 atm, where the system is rigid and loses elasticity.

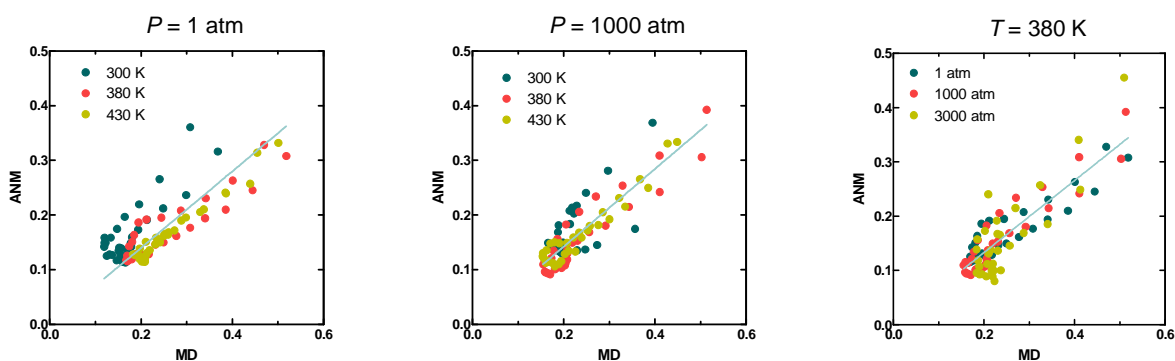


Figure 4.4. Normalized RMSD averaged over all chains obtained from ANM and MD simulation for different temperatures at 1 atm, 1000 atm and for different pressures at 380 K.

The correlations of the RMSD values of chains obtained from ANM and MD are in increasing trend for higher temperatures for both 1 atm and 1000 atm case and

decreasing trend for higher pressure values when the temperature is fixed to 380 K (see figure 4.5).

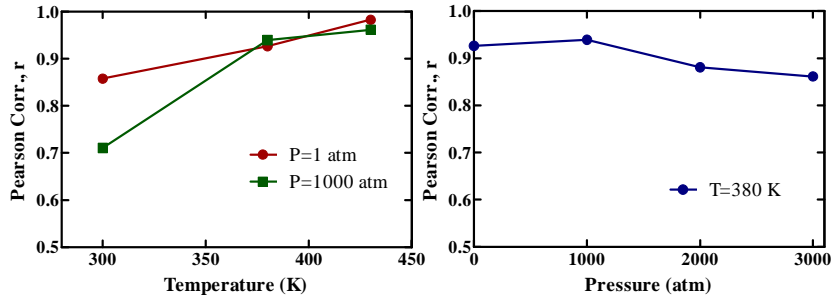


Figure 4.5. Pearson correlation factors, r , of chain fluctuations between those calculated from MD simulations and ANM

Due to the high correlations between MD obtained fluctuations and ANM predictions; we use this data to calculate the effective spring constant between chain units. The spring constants (or average stiffness) of the bonds which are related to the average fluctuations of the atoms are obtained from the ratio of trace of covariance matrix, C , (equation 2.13) to the average of RMS-fluctuations obtained from MD simulations multiplied by the prefactor $3 k_B T$:

$$\gamma = 3k_B T \frac{\text{tr}(C_{ii})}{\langle \Delta R^2 \rangle_{MD}} \quad (4.3)$$

As seen in the figure 4.6a, linear fit to the spring constants of the atoms has a negative slope indicating that spring constants are inversely proportional to temperature, whereas for the pressure set (figure 4.6b) spring constants are linearly increasing as the temperature increases. In fact, when the temperature is low, the atoms in the system fluctuate less from their equilibrium point and give rise to lower value of stiffness, and when the pressure is increased, the system goes in a more compact form with motions in a smaller volume with higher frequency resulting in higher stiffness.

4.3. Predicting the Second Virial Coefficients

The second virial coefficient (b_2), which is an experimentally obtainable thermodynamic quantity, was predicted by ANM. Second virial coefficient was obtained from Hessian matrix (derivation details are in Appendix B);

$$b_2^{ANM} = \frac{-\gamma}{6Nk_B T} R^T (H - D) R \quad (4.4)$$

where H is the Hessian matrix, R is the coordinate vector of all atoms relative to center of mass of the system, D is the identity matrix. b_2 may also be calculated from the RDF;

$$b_2^{RDF} = \frac{2\pi}{3V} \int_0^\infty g'(r) r^3 dr \quad (4.5)$$

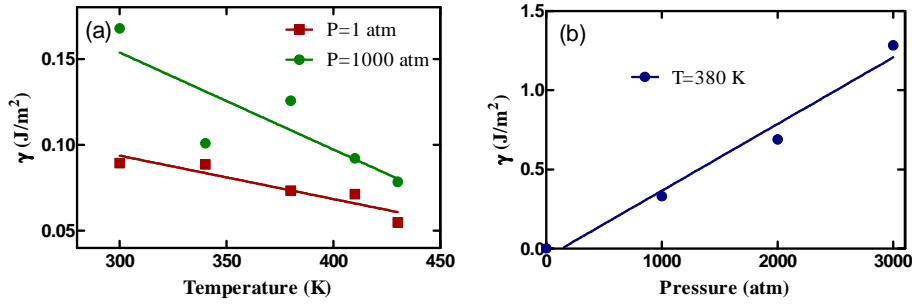


Figure 4.6. Comparison of spring constants for different (a) pressure and (b) temperature sets.

where V is the volume of the simulated system and $g'(r)$ is the derivative of the RDF with respect to r . In the equation 4.5, the small deviations in the RDF give rise to big fluctuations during the integration, so we obtain an equivalent form using integration by parts, leading to,

$$b_2^{RDF} = \frac{2\pi}{3V} (r^3|_0^{r_{cut}} - \int_0^{r_{cut}} g(r) 3r^2 dr) \quad (4.6)$$

where r_{cut} is taken as 20 Å (approx. half of the simulation box length).

The calculated values of b_2 from different sets of temperatures and pressures are listed in the table 4.1. Although the predicted values obtained by ANM have lower values than the calculated values from the MD simulations, when normalized, the fitted

lines are highly correlated and behave qualitatively similar. For fixed values of pressures, 1 atm and 1000 atm, normalized b_2 decrease as the temperature is increased (figure 4.7a and figure 4.7b), and when the pressure is increased for fixed temperature for 380 K, we see a positive correlation with respect to pressure (figure 4.7c). Normalization in figures 3.10a-c is carried out such that the maximum value is set to 1 and the minimum to 0 in each case.

Table 4.1. Second virial coefficients obtained from RDF and ANM construction

Temperature (K)	Pressure (atm)	box dimension (Å)	b_2^{RDF}	b_2^{ANM}
300	1	47.9	437.2	64.8
340	1	48.4	367.4	57.4
380	1	48.9	317.1	41.6
410	1	49.6	280.6	37.6
430	1	50.2	259.5	27.6
300	1000	46.5	482.9	120.0
340	1000	46.9	413.7	63.7
380	1000	47.1	363.3	70.7
410	1000	47.4	329.7	47.6
430	1000	47.7	307.5	39.1
380	1	48.9	317.1	41.6
380	1000	47.1	363.3	70.7
380	2000	46.5	382.9	384.6
380	3000	45.9	400.5	723.1

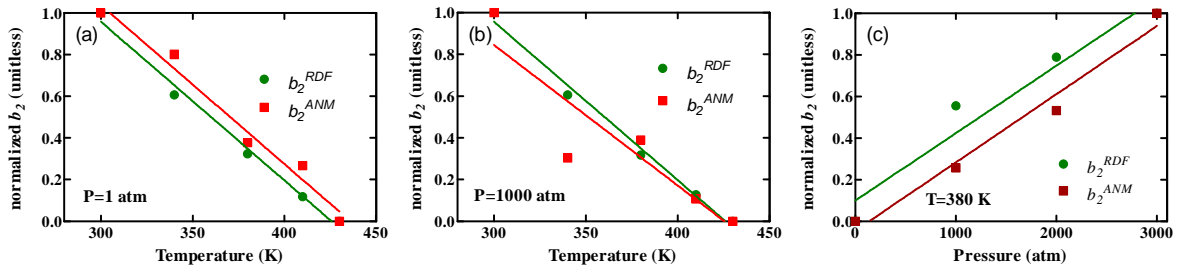


Figure 4.7. Normalized second virial coefficients at (a) constant pressure of 1 atm, (b) constant pressure of 1000 atm, (c) and at constant temperature of 380 K

5. LINEAR VISCOELEASTIC PROPERTIES OF POLYBUTADIENE MELTS PROBED BY NANOCLUSTERS: MD SIMULATIONS AND EXPERIMENTS

5.1. Radial Distribution Function (RDF) of Polymer with Nanoclusters

Radial distribution functions calculated from the MD simulations are shown in figures 5.1, 5.2 and 5.3. The effect of atom type, temperature and cluster size to the configuration of the system was investigated. At short distances (less than atomic diameter) $g(r)$ is zero. This is due to the strong repulsive forces. At long distances, $g(r)$ approaches to a constant value which indicates there is no long-rang order.

In figure 5.1, pair correlations of two different atomic types are compared for the same temperature (330 K) and same nanocluster size ($N = 10$ atoms). The first (and large) peaks occurs at 1.54 Å and 1.34 Å corresponding respectively to sp^3 and sp^2 type atoms. The radial distribution function then has four peaks, corresponding to higher coordination shells, which have much smaller intensity compared to the first peak (resulting from bonding in consecutive repeat units). Since the polymer systems in our simulations have % 100 *cis* content, second peak of sp^2 have smaller probability when compared to sp^3 which is in a more rigid environment. In figure 5.2, we do not see much effect of nanocluster size on the sp^2 RDF; however, there are small perturbations in the first three peaks of sp^3 RDF. Similarly there are small perturbations to the sp^2 and sp^3 type atomic RDFs when the temperature is changed (figure 5.3). In particular, long range order of sp^3 type atoms are affected more than the sp^2 type atomic pair distributions.

5.2. Diffusion Coefficient and Zero-Shear Viscosity

The calculated values of diffusion constants for temperatures 330 K, 380 K and 430 K and the curves obtained from these tables and linear fits to obtain zero-shear viscosities are given in the Appendix D.

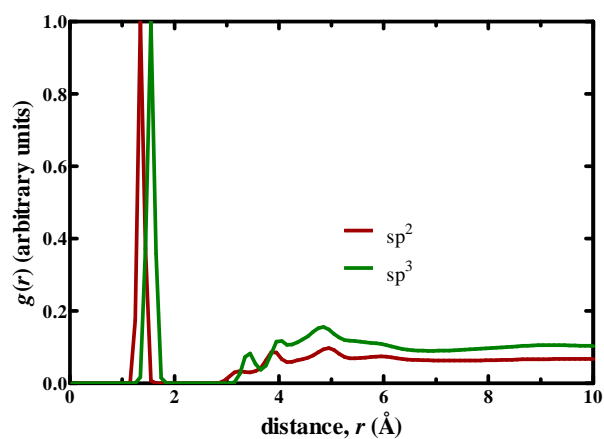


Figure 5.1. Comparison of RDF of sp^3 and sp^2 atoms at $T=330$ K

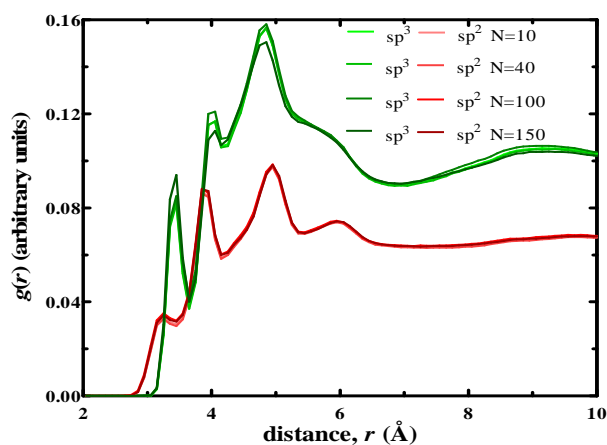


Figure 5.2. Cluster size effect on the RDF of sp^3 and sp^2 atoms at $T=330$ K

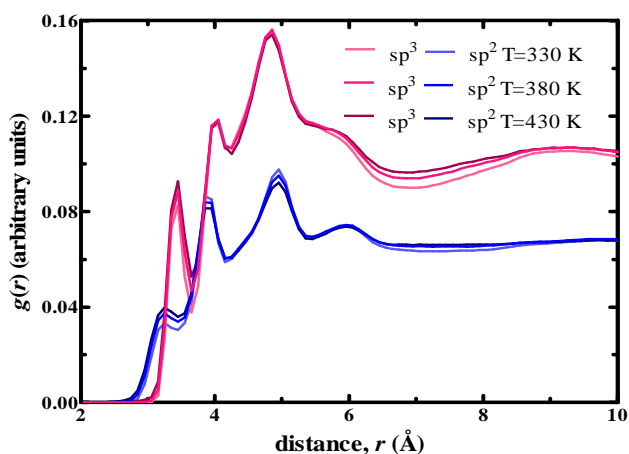


Figure 5.3. Effect of temperature to the RDF of sp^3 and sp^2 atoms for the system with nanocluster of 10 atom-size

Viscosities that are obtained from four different simulation sets as well as experiments on PBD described in section 2.3.6 are plotted in figure 5.4. Both viscosities from simulation and experiments have increasing logarithmic character as the temperature decreases. Calculated values are close to the experimental values except at 280 K at which experimental values is approximately 3 times larger.

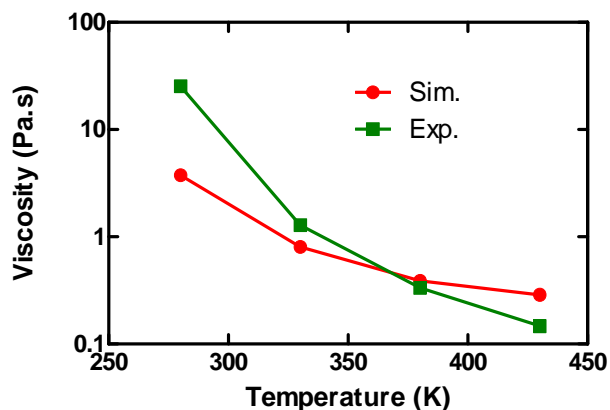


Figure 5.4. Comparison of zero-shear viscosity with respect to temperature obtained from simulations and experiment

5.3. Dynamical Properties

Correlation times, τ_c , (equation 2.28) of C-H bond vectors of simulation at four different temperatures were compared in figure 5.5 with the ^{13}C NMR experimental data from the literature [84]. In figure 5.5, experimental τ_c values belong to high cis-content-polybutadiene (%93 *cis*, %3 *trans* and %4 *vinyl*). The values obtained from simulation are in good agreement qualitatively with the experimental values, except at 280 K where the deviation is larger. C-H bond rotations are approximately 2.5 orders of magnitude more active at 430 K when compared to the value at 280 K.

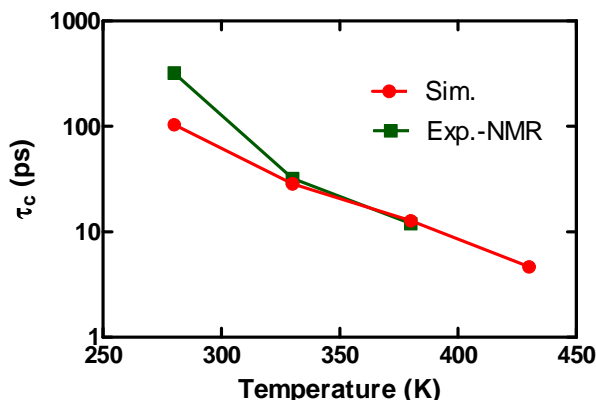


Figure 5.5. Comparison of correlation time, τ_c , of simulation and experiment with respect to temperature calculated from probes of $N = 10$ atoms

In order to see the effect of temperature and the size of the nanocluster on the dynamical behavior of polymer chains, we obtained the residence times, τ_r (equation 2.30) with respect to size and temperature (figure 5.6a,b). We see that as the temperature increases, residence time of the chains decreases. At higher temperatures, the chains spend less time at the surface of the nanocluster. In addition, for the larger nanocluster sizes, chains spend more time in the vicinity of the probe, which indicates additional interactions with the polymer chains. Conversely, such a size dependent behavior is not observed for the relaxation times of these chains. τ_r decreases from ~ 210 ps to ~ 130 ps as the temperature increase from 280 K to 430 K, whereas it increases two-fold (~ 100 ps to ~ 200 ps) as the size of the nanocluster increases from ~ 3 to ~ 7 nm. From the results it is observed that 150 K difference in the temperature corresponds to 4 Å difference of particle radius.

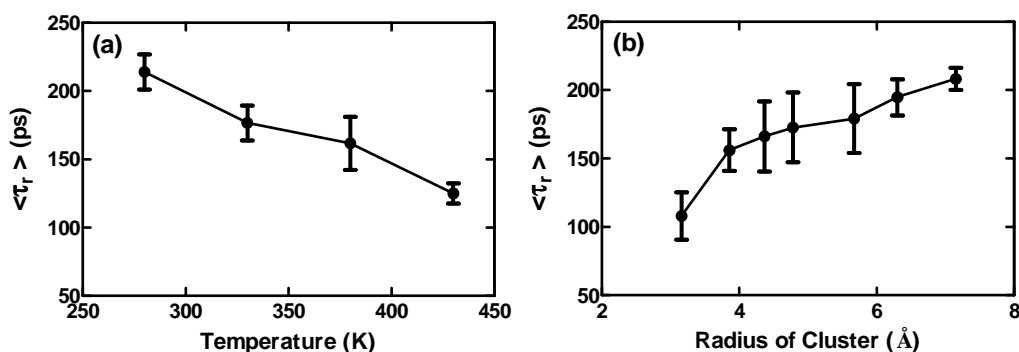


Figure 5.6. (a) Temperature (size averaged) and (b) size dependence (temperature average) of residence times (τ_r)

To see the effect of vdw interaction strength ($-\epsilon_{\text{Si-C}}$) on the dynamical behaviour of interacting nodes (the nodes within one vdw length of the nanocluster surface) of PBD, $-\epsilon_{\text{Si-C}}$ is increased from $-\epsilon_{\text{Si-C}}=0.1$ kcal/mol up to $-\epsilon_{\text{Si-C}}=1.5$ kcal/mol, where the standard value in the previous sets of simulations was $-\epsilon_{\text{Si-C}}=0.3$ kcal/mol. Both τ_r and τ_c are calculated from the dataset of $T = 330$ K and $N = 150$ atoms. From the figure 5.7a, it is observed that τ_r has an asymptotic exponential association type behaviour. τ_r show this character apparently by increasing two-fold from ~ 100 ps (lowest interaction strength) to ~ 200 ps (highest interaction strength). In figure 5.7b, τ_c increases from 20 ps (pure PBD) to 80 ps until $-\epsilon_{\text{Si-C}}=0.75$ kcal/mol and drops to below 70 ps until $-\epsilon_{\text{Si-C}}=1.5$ kcal/mol. Presence of the cluster slows down the node orientation movement, therefore the relaxation rate. This leads to the sticking of the nodes to the nanocluster surface.

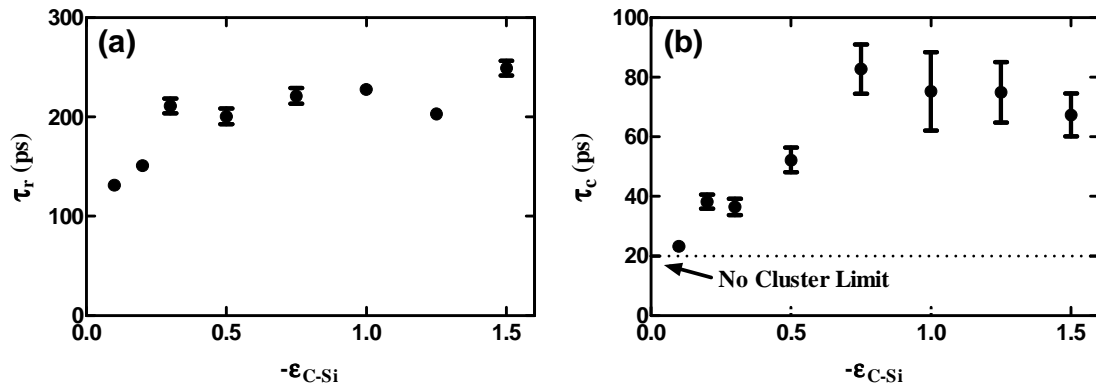


Figure 5.7. (a) Effect of vdw interaction strength to τ_r and (b) τ_c at $T=330$ K and $N=150$ atoms

5.4. Mechanical Properties

In this section, we investigate the effect of four different parameters (vdw interaction strength, nanocluster size, temperature and MW) on the mechanical behavior of the polymer nanocomposite. To see the effect of nanocluster size, we set $-\epsilon_{\text{Si-C}}=0.3$ kcal/mol and $T=330$ K. From the figure 5.8a, it is seen that from very small sizes ($N=10$ atoms) up to moderate sizes ($N=70$ atoms and $N=100$ atoms), K increases $\sim 5\%$ but drops to the starting K value of $N = 10$ atoms as the nanocluster size is further increased to $N=150$ atoms. So, from practical point of view, we can assume that K is not much

affected by the size of the nanocluster. And for to observe the effect of vdw interaction strength on K , we set $T=330$ K and $N=150$ atoms, and we have calculated the K values, for a set of vdw interaction strengths ($-\epsilon_{\text{Si-C}}=0.1, 0.2, 0.3, 0.5, 0.75, 1.0, 1.25$ and 1.5 kcal/mol). In figure 5.8b, K does not change until $-\epsilon_{\text{Si-C}}=0.75$ kcal/mol and starts to increase linearly until $-\epsilon_{\text{Si-C}}=1.5$ kcal/mol. This increase is approximately 8%.

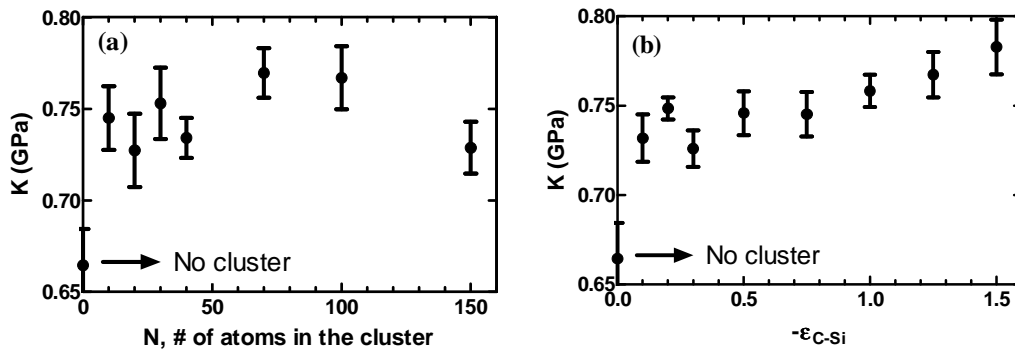


Figure 5.8. (a) Effect of cluster size and (b) vdw interaction strength to bulk modulus calculated from inverse of κ_T .

The effect of the other parameter of interest, molecular weight, was studied by increasing the chain size 4-fold by keeping T at 330 K and N at 150 atoms. In figure 5.9, K is plotted with respect to vdw interaction strength for two sets of molecular weights. Increasing the MW caused a slight increase in K . It is observed that this increase does not exceed %20.

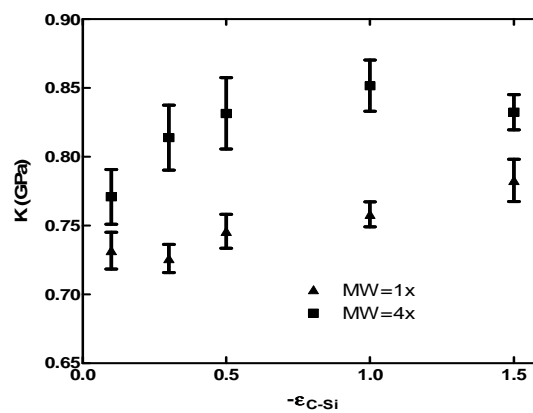


Figure 5.9. Effects of vdw interaction strength, MW to bulk modulus that are calculated from inverse of κ_T .

To see the effect of parameters of interest on shear modulus, G , a different method (see section 2.3.3) was used. In addition to simulation sets indicated above, three more simulations with molecular weights of the PBD that are $\frac{1}{4}$, $\frac{1}{2}$, 2, 4 and 8 times that of the original system are carried out. From each simulation, ten snapshots are obtained from the last 5 ns piece of the simulation (each 0.5 ns apart) for further analysis in the MS Program. The averaged values of G over these snapshots for different parameters are plotted with their standard error in figure 5.10. In all of the figures, G values are always approximately 2-fold less than the K values (see figure 5.8) which is characteristic for polymers. G values have an increasing trend with the with increasing MW and ϵ , whereas G has a bump at $N=70$ atoms and an increase from $N=100$ atoms to $N=150$ atoms. The characteristic curves of G have similar behaviour as we have seen for K (see figure 5.8) except for the case of $N=150$ atoms. For $N=150$ atoms, G starts to increase as opposed to decreasing trend of K .

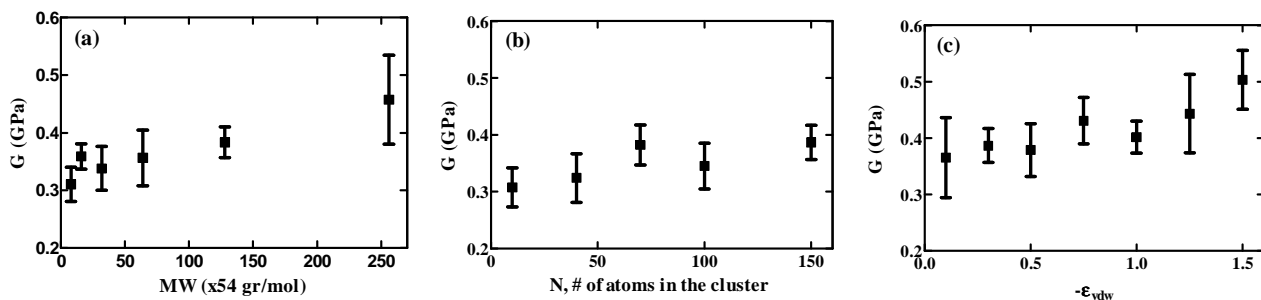


Figure 5.10. Effect of (a) molecular weight, (b) nanocluster size, and (c) vdW interaction strength on shear modulus.

5.5. Glass Transition Temperature

In order to calculate T_g , the PBD system with $N = 150$ atoms with $-\epsilon_{Si-C} = 0.1$ kcal/mol (weak), $-\epsilon_{Si-C} = 0.3$ kcal/mol (normal) and $-\epsilon_{Si-C} = 1.5$ kcal/mol (strong) and pure PBD are simulated for the temperatures from 130 K to 200 K with 5 K step and from 200 K to 240 K with 10 K step. Changes in specific volume with temperature are shown in figure 5.11. For each type of systems, curves have two kinks: one small peak at temperatures less than 150 K and one apparent peak between 160 K and 180 K. The

temperatures corresponding to the latter transition are 176 K for the pure PBD system, 177 K for the system with the weak interaction strength, 184 K for the system with the standard interaction strength and 178 K for the system where there is strong interaction between the nanocluster and the PBD chains. According to these results, T_g increases as the nanoclusters are introduced to the polymer melt and decreases as the interaction strength increases further from the standard value.

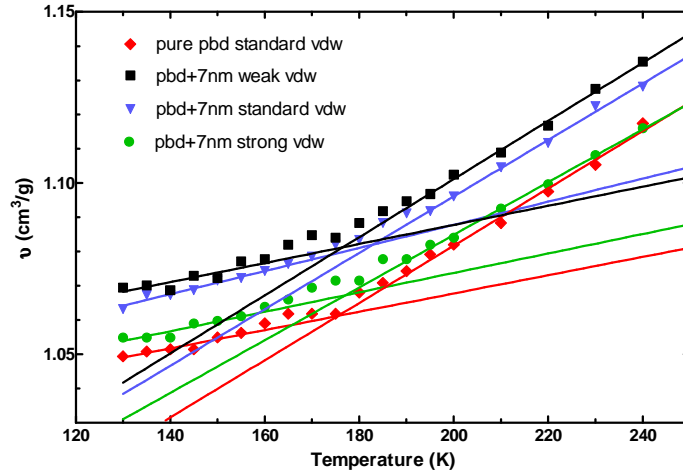


Figure 5.11. Change in specific volume with respect to temperature for predicting T_g

In figure 5.12, the effect of MW on T_g is obtained from from three sets of molecular weights; MW=1x, 4x and 8x. As the MW increases, T_g is observed to shift to higher temperatures according to the Fox-Flory empirical equation [99]:

$$T_g(MW) = T_g(\infty) - \frac{A}{MW} . \quad (5.1)$$

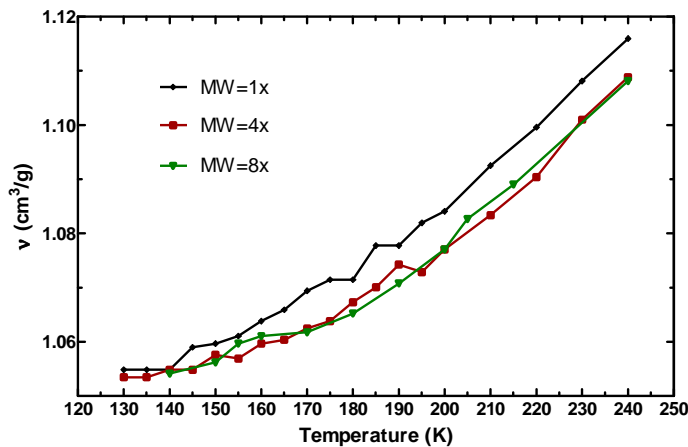


Figure 5.12. Change in specific volume with respect to MW for $-\epsilon_{Si-C} = 1.5$ kcal/mol (strong vdw interaction)

6. CONCLUSION AND FUTURE WORK

In this work we first studied the extent of predictions of elastic network models on the well-studied protein systems. We then sought to understand the extent of applicability of Anisotropic Network Model (ANM) to oligomeric systems, exemplified by polybutadiene melts. We then used nanoclusters to probe the linear viscoelastic properties of these melts. Finally, we used these nanopores to manipulate properties of polymers. These include mechanical strength, which is directly correlated with force constants derived by ANM, as well as the glass transition temperature.

In the first part of the thesis, the extent of predictions of elastic network models on the well-studied protein systems is studied. Despite their different topological structures and sizes, a statistical analysis of a large number of folded proteins leads to common features. In particular, the radial and angular distribution functions provide the degree of (in)homogeneity in the protein as well as a quantitative description of the location of the coordination shells. Depth dependent analysis shows that the densely packed core region of the protein has a different local structure built around it compared to its surface. In the core of the protein, the second neighbors have a non-random distribution that is more pronounced than the first neighbors. In the surface residues, the reverse is observed (figure 3.1b).

Calculations at a variety of cut-off distances used in network construction reflect that the dimensionality of the system approaches that of regular crystals where $g(\omega)$ scales with ω^2 only at unrealistically high r_c values (figure 3.2b). The modal spectrum resembles that obtained from all-atom calculations with realistic atom-atom interaction potentials in the region above the second coordination shells up to a cut-off distance of 16 Å (figure 3.2a). At this threshold, the spectral dimension shifts from the region of $d_s = 1-2$ to above 2, accompanied by a crossover in its rate of change (figure 3.2b).

Network constructed by using Voronoi tessellations, on the other hand, fail to correctly define the local interactions while they successfully incorporate the long-range pairwise interactions. In particular, the mode distributions (figure 3.2a) and the spectral

dimensions measured at the slow mode region (figure 3.2b) do not represent the experimentally and theoretically well-characterized shapes for proteins. Therefore, these network models will provide misleading information on the properties that rely mostly on local interactions (e.g. residue fluctuations, figure 3.3). On the other hand, they are expected to be very effective in forecasting properties that depend on a correct incorporation of the long-range contacts, as was recently demonstrated by their success in predicting the folding rates of two-state proteins [100, 101]

In the second part, in order to understand the extent of applicability of ANM to polymeric systems, we have successfully simulated bulk model of *cis*-1,4-PBD over a range of pressures and temperatures well above its glass transition temperature ($T_g \sim 175$ K). With MD simulations, we are able to analyze and obtain useful predictions for the fluctuations, spring constants and second virial coefficients at different pressures and temperatures. Macroscopic properties such as $\langle R^2 \rangle$, C_n , v , κ_T are obtained *a priori* to check whether or not the system fully relaxes and predicts similar values to the experimentally measured ones obtained for bulk PBD systems. By predicting thermodynamic properties and showing correlation of ANM with the experiments in the literature as well as MD simulation results, we have assessed the validity and range of applicability of ANM.

The simulated systems have very similar structural and conformational properties with small differences in the second and third nearest neighbors as confirmed by RDFs. However, these small local differences and arrangements result in considerable differences in thermodynamical properties which are estimated qualitatively by applying ANM to the relaxed coordinates of the system obtained from MD simulations.

RMSD values of the chains obtained by ANM and MD are highly correlated, yielding values in the range 0.7 - 0.95. When averaged over all atoms, the trends of these RMSD values from different temperatures and pressures are in good agreement with the expected qualitative trends with the exception of highest pressure studied, 3000 atm and the lowest temperature studied, 300 K. Similarly, values of spring constants and the second virial coefficients estimated by ANM are qualitatively correlated with the values obtained from MD directly.

In the third part of the thesis, we use nanoclusters to probe the linear viscoelastic properties of these melts and to manipulate properties of polymers by playing parameters such as temperature, size, vdw interaction strength between the nanocluster and polymer. First, we calculated the diffusion coefficients of the polymer and by fitting these coefficients to the Einstein-Stoke Equation, zero-shear viscosity of the polymer is predicted. The viscosity results have been compared with those for %60 cis-content PBD chains of similar molecular weight measured by rotational viscosimeter. The estimated viscosity results have close values to the experimental results, having the expected logarithmic trend. The relaxation times of C-H vectors are also in very good quantitative agreement with NMR measured values, confirming that the united atom force field used in the simulations well-describes the dynamics of the real system.

RDF for different temperature and nanocluster sizes was also extracted in order to see the effect of these parameters on the configurational properties. It is observed that despite the size and temperature slightly modifies the different coordination shells, there is no obvious change in the RDF in the bulk of the system.

In order to see the underlying mechanism of dynamical behaviour of polybutadiene chains in the vicinity of the nanoclusters and the relaxation times of chain nodes (sp^2 atoms in the butadiene monomer), residence time (τ_r) and correlation time (τ_c) have respectively been calculated from MD simulations. Escape and correlation times reach a plateau as the interaction strength increases, because the polymer chains are stick to the surface more tightly and their translational and orientational movements are much more restricted.

It is also possible to manipulate mechanical properties by tuning the interaction strength of the nanoclusters with the chains. Approximately 7 % increase in the bulk modulus and 25 % increase in the shear modulus are obtained by changing the vdw interaction strength from weak to strong. Furthermore, MW affects both bulk and shear moduli. However, increasing the size of the nanoclusters has an increasing effect on both bulk and shear modulus up to $N=70$ atoms, further increase of the size decreases the bulk modulus to the values of the smaller sizes and increases the shear modulus further. From practical point of view, we can assume that K is not much affected by the

size of the nanocluster, whereas K linearly increases as the interaction strength increases from normal to strong values.

T_g increases as the nanoclusters are introduced to the polymer melt and decreases as the interaction strength increases away from the standard value. T_g is increased from ~ 176 K for pure PBD up to ~ 184 K for the standard interaction strength. T_g also have an increasing trend by MW in accordance to theoretical expectations.

For future work, first in order to obtain the change in chain order near the nanocluster surface, both translational order, as quantified by RDF, and orientational order parameters will be extracted for different set of parameters. The latter in fact an extension of ADF, developed in Chapter 3, and has been studied in detail for a series of amorphous materials (ref Steinhardt 1983). These atomistic order details will be used to understand the underlying mechanism that lead to the observed mechanical and dynamical property variations in the bulk polymer. In addition, the observed effect of vdw strength on moduli and T_g will be explained using thermodynamical arguments based on entropy-enthalpy balance. The current approach may further be applied to polymers with different chain architecture such as copolymers, those incorporating ring groups and branching. Finally, the interaction between the nanocluster and polymer chains may be modified by adding explicit or partial charges to the nanocluster atoms, or direct covalent bonds to the chains to see if we can further enhance the modulus or other macroscopic properties.

APPENDICES

APPENDIX A: Application of Periodic Boundary Conditions (PBC)

To implement PBC in practice, at least two steps are needed. The first is to have an atom (or a node) which leaves the simulation cell on one side to enter back from the other side. This is of course a simple operation, and could be implemented in the code by three *if statements*: e.g. (for the x dimension, assuming an orthogonal unit cell centered on the origin). And second is to make sure that every distance between atoms has a length and direction which corresponds to the minimum image criterion. This can be achieved in the x direction (which should be repeated in all 3 dimensions) as follows:

<pre> <i>f</i> (<i>periodicx</i>) <i>then</i> <i>if</i> ($x < -xsize/2.0$) $x=x+xsize$ <i>if</i> ($x \geq xsize/2.0$) $x=x-xsize$ <i>endif</i> </pre>	<pre> <i>if</i> (<i>periodicx</i>) <i>then</i> $dx = x(j) - x(i)$ <i>if</i> ($dx > xsize/2.0$) $dx = dx - xsize$ <i>if</i> ($dx \leq -xsize/2.0$) $dx = dx + xsize$ <i>endif</i> </pre>
--	---

Handling PBC in Constrcuting Connectivity and Hessian Matrices

Figure A.1 depicts the graphical representation of the application of PBC to 2D box with 4 interacting points. The corresponding Connectivity (Kirchhoff) Matrix is shown in the inset. The total number of connections of the particle 3 is increased one more in the diagonal entry if it is within the cut-off distance after having mirror-image in the x -direction. The non-diagonal (3,4) and (4,3) entries does not change. Similarly, only the diagonal elements of the Hessian Matrix are increased as the mirrored particles come to the interaction range of the other particles within the cut-off value. (For 3D the mirror image is calculated in 2 direction in each axis

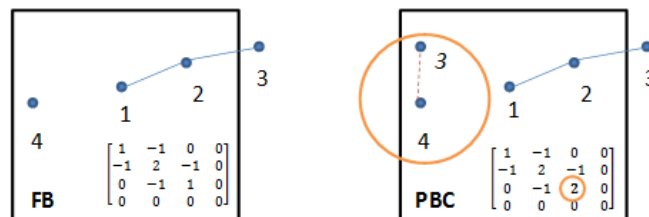


Figure A.1. Graphical representations of Free Boundary (FB) and Periodic Boundary Conditions (PBC) and corresponding Connectivity Matrices (inset)

APPENDIX B: Derivation of Second Virial Coefficient (b_2) from ANM

The pressure of a system consists of two terms; ideal (thermodynamical) term and the virial term.

$$P = P_{ideal} + P_{virial} = \frac{Nk_B T}{V} - \frac{1}{3V} \sum_{i=1}^{N-1} \sum_{j=i+1}^N f_{ij} \cdot r_{ij} \quad (\text{B.1})$$

In network models, force on i - j pair is given by $-\gamma_{ij} \Delta R_{ij}$; thus, the $(f_{ij} \cdot r_{ij})$ term is;

$$= -\gamma_{ij} [(R_j - R_i) - (R_{j0} - R_{i0})] \cdot (R_j - R_i) \quad (\text{B.2})$$

$$= \gamma_{ij} (R_{ij})^2 + \gamma_{ij} (R_{ij}^0 \cdot R_{ij}) \quad (\text{B.3})$$

$$= \gamma_{ij} (R_{ij})^2 \quad (\text{B.4})$$

For the whole system, the virial coefficient becomes;

$$b_2^{ANM} = \frac{-\gamma}{6Nk_B T} R^T (H - D) R \quad (\text{B.5})$$

APPENDIX C: Derivation of Isothermal Compressibility (κ_T) from ANM

Using simple elastic network model potential ($u(r) = \Delta R^T \Gamma \Delta R^T$) for the interacting pairs (or nodes), the isothermal compressibility is equal to equation C.1. Upon integration, we obtain the relation of κ_T to the multiplication of the eigenvalues, omitting those equal to zero due to the pseudo-inversion, obtained from Kirchoff (Connectivity) Matrix.

$$\kappa_T = \frac{1}{kT} \int_v \exp\left(-\frac{\Delta R^T \Gamma \Delta R^T}{kT}\right) dv \quad (\text{C.1})$$

$$= \frac{1}{kT} \left(\frac{\pi^N}{\det(\Gamma/kT)}\right)^{3/2} \quad (\text{C.2})$$

$$= \frac{1}{kT} \left(\frac{\pi^N}{\prod_{i=1,N} \frac{\lambda_i}{kT}}\right)^{3/2} \quad (\text{C.3})$$

$$= \frac{1}{kT} \left(\frac{kT}{\gamma}\right)^{3/2} \frac{\pi^{3N/2}}{(\prod_{i=1,N} \lambda_i)^{3/2}} \quad (\text{C.4})$$

APPENDIX D: Details of the Diffusion Coefficients and Viscosity Predictions

Table D.1. Details of the diffusion coefficients of PBD+Cluster at $T=330$ K

cluster size (# of atoms)	r (Å)	1/r	slope	y- intercept	diff.coef.
10	3.162243	0.316231	1.003	-4.216	1.01356E-07
20	3.858489	0.259169	1.002	-4.414	6.42464E-08
30	4.372635	0.228695	1.003	-4.356	7.34258E-08
40	4.778822	0.209257	1.003	-4.18	1.10116E-07
70	5.6718	0.176311	1	-4.365	7.19198E-08
100	6.303312	0.158647	1.004	-4.741	3.02586E-08
150	7.147039	0.139918	1.002	-4.626	3.9432E-08

Table D.2. Details of the diffusion coefficients of PBD+Cluster at $T=380$ K

cluster size (# of atoms)	r (Å)	1/r	slope	y- intercept	diff.coef.
10	3.162243	0.316231	1.018	-3.767	2.85003E-07
20	3.858489	0.259169	1.001	-3.948	1.87866E-07
30	4.372635	0.228695	0.9949	-3.985	1.72524E-07
40	4.778822	0.209257	0.8979	-3.219	1.00658E-06
70	5.6718	0.176311	1.001	-4.082	1.3799E-07
100	6.303312	0.158647	1.003	-4.847	2.37055E-08
150	7.147039	0.139918	1.001	-4.609	4.10061E-08

Table D.3. Details of the diffusion coefficients of PBD+Cluster at $T=430$ K

cluster size (# of atoms)	r (Å)	1/r	slope	y- intercept	diff.coef.
10	3.162243	0.316231	1.001	-3.522	5.01013E-07
20	3.858489	0.259169	1.001	-3.675	3.52248E-07
30	4.372635	0.228695	1.001	-3.981	1.7412E-07
40	4.778822	0.209257	1.002	-4.092	1.34849E-07
70	5.6718	0.176311	1.002	-4.089	1.35784E-07
100	6.303312	0.158647	1.002	-4.092	1.34849E-07
150	7.147039	0.139918	1.001	-4.462	5.7524E-08

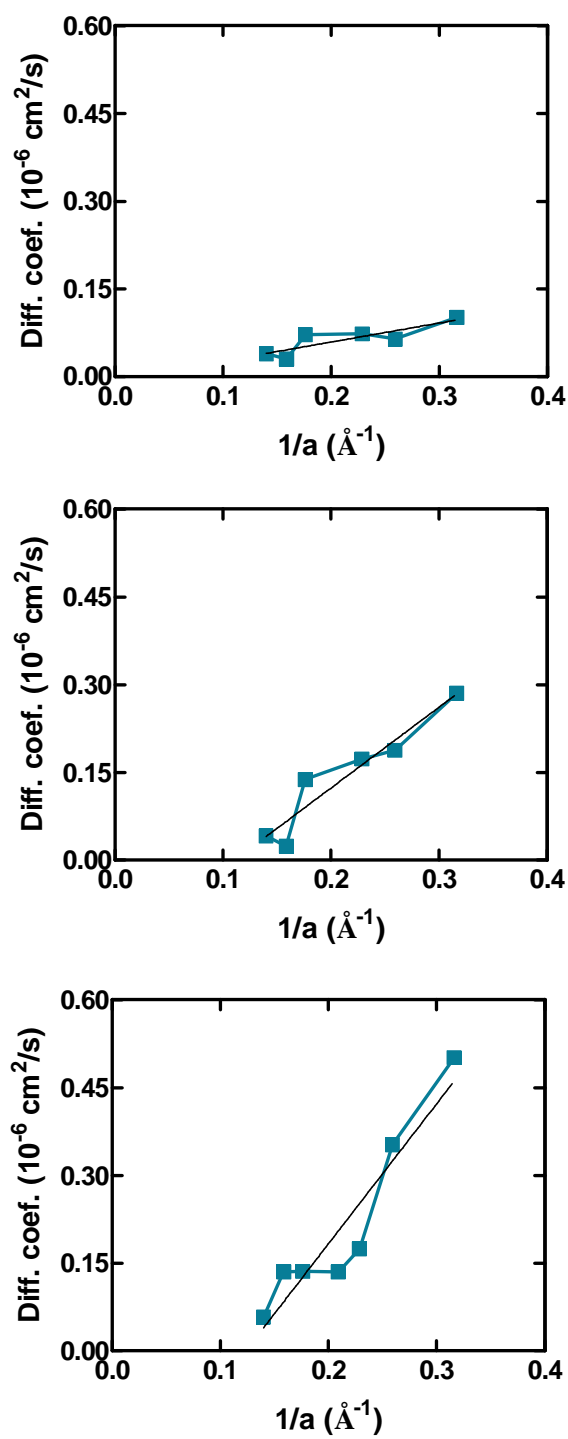


Figure D.1. Predictions of zero-shear viscosities from diffusion coefficients for $T=330$ K, 380 K, and 430 K

REFERENCES

1. Flory, P.J., *Principles of Polymer Chemistry*. 1953, Itacha: Cornell University.
2. deGennes, P.G., *Scaling Concepts in Polymer Physics*. 1979, London, UK: Cornell University Press.
3. Freed, K.F., *Renormalization Group Theory of Macromolecules*. 1987, New York, USA: Wiley.
4. M. Doi, S.F.E., *The Theory of Polymer Dynamics*. 1986, London, UK: Oxford University Press.
5. Binder, K., *Monte Carlo and Molecular Dynamics Simulations in Polymer Science*. 1995, New York, USA: Oxford University Press.
6. J. P. Hansen, I.R.M., *Theory of Simple Liquids*. 1976, London, UK: Academic Press.
7. Hoogerbrugge, P.J. and J.M.V.A. Koelman, *Simulating Microscopic Hydrodynamic Phenomena with Dissipative Particle Dynamics*. Europhysics Letters, 1992. **19**(3): p. 155-160.
8. Espanol, P. and P. Warren, *Statistical-Mechanics of Dissipative Particle Dynamics*. Europhysics Letters, 1995. **30**(4): p. 191-196.
9. Nikunen, P., I. Vattulainen, and M. Karttunen, *Reptational dynamics in dissipative particle dynamics simulations of polymer melts*. Physical Review E, 2007. **75**(3).
10. Espanol, P., *Dissipative particle dynamics for a harmonic chain: A first-principles derivation*. Physical Review E, 1996. **53**(2): p. 1572-1578.
11. Symeonidis, V., G.E. Karniadakis, and B. Caswell, *Dissipative particle dynamics simulations of polymer chains: Scaling laws and shearing response compared to DNA experiments*. Physical Review Letters, 2005. **95**(7).
12. Ozen, A.S., U. Sen, and C. Atilgan, *Complete mapping of the morphologies of some linear and graft fluorinated co-oligomers in an aprotic solvent by dissipative particle dynamics*. Journal of Chemical Physics, 2006. **124**(6).
13. Can, H., G. Kacar, and C. Atilgan, *Surfactant formation efficiency of fluorocarbon-hydrocarbon oligomers in supercritical CO₂*. Journal of Chemical Physics, 2009. **131**(12).
14. Erman, B., A. Kloczkowski, and J.E. Mark, *Chain Dimensions and Fluctuations in Random Elastomeric Networks .2. Dependence of Chain Dimensions and Fluctuations on Macroscopic Strain*. Macromolecules, 1989. **22**(3): p. 1432-1437.
15. Kloczkowski, A., J.E. Mark, and B. Erman, *Chain Dimensions and Fluctuations in Random Elastomeric Networks .1. Phantom Gaussian Networks in the Undeformed State*. Macromolecules, 1989. **22**(3): p. 1423-1432.
16. Ozen, A.S., G. Kacar, and C. Atilgan, *Mapping and Reverse-Mapping of the Morphologies for a Molecular Understanding of the Self-Assembly of Fluorinated Block Copolymers*. Journal of Physical Chemistry C, 2010. **114**(1): p. 370-382.
17. Soyer, A., et al., *Voronoi tessellation reveals the condensed matter character of folded proteins*. Physical Review Letters, 2000. **85**(16): p. 3532-3535.
18. Raghunathan, G. and R.L. Jernigan, *Ideal architecture of residue packing and its observation in protein structures*. Protein Science, 1997. **6**(10): p. 2072-2083.

19. Baysal, C., A.R. Atilgan, and P. Akan, *Small-world communication of residues and significance for protein dynamics*. Biophysical Journal, 2004. **86**(1): p. 85-91.
20. Liang, J. and K.A. Dill, *Are proteins well-packed?* Biophysical Journal, 2001. **81**(2): p. 751-766.
21. Zhang, J.F., et al., *Origin of scaling behavior of protein packing density: A sequential Monte Carlo study of compact long chain polymers*. Journal of Chemical Physics, 2003. **118**(13): p. 6102-6109.
22. Benavraham, D., *Vibrational Normal-Mode Spectrum of Globular-Proteins*. Physical Review B, 1993. **47**(21): p. 14559-14560.
23. Bahar, I., et al., *Vibrational dynamics of folded proteins: Significance of slow and fast motions in relation to function and stability*. Physical Review Letters, 1998. **80**(12): p. 2733-2736.
24. Atilgan, A.R., et al., *Anisotropy of fluctuation dynamics of proteins with an elastic network model*. Biophysical Journal, 2001. **80**(1): p. 505-515.
25. Bahar, I. and A.J. Rader, *Coarse-grained normal mode analysis in structural biology*. Current Opinion in Structural Biology, 2005. **15**(5): p. 586-592.
26. Bahar, I., et al., *Global Dynamics of Proteins: Bridging Between Structure and Function*. Annual Review of Biophysics, Vol 39, 2010. **39**: p. 23-42.
27. Sternstein, S.S. and A.J. Zhu, *Reinforcement mechanism of nanofilled polymer melts as elucidated by nonlinear viscoelastic behavior*. Macromolecules, 2002. **35**(19): p. 7262-7273.
28. Cui, Q., *Normal Mode Analysis: Theory and Applications to Biological and Chemical Systems*. 2006, Florida USA: Chapman & Hall/CRC.
29. Bahar, I., A.R. Atilgan, and B. Erman, *Direct evaluation of thermal fluctuations in proteins using a single-parameter harmonic potential*. Folding & Design, 1997. **2**(3): p. 173-181.
30. Delarue, M. and Y.H. Sanejouand, *Simplified normal mode analysis of conformational transitions in DNA-dependent polymerases: the Elastic Network Model*. Journal of Molecular Biology, 2002. **320**(5): p. 1011-1024.
31. Tirion, M.M., *Large amplitude elastic motions in proteins from a single-parameter, atomic analysis*. Physical Review Letters, 1996. **77**(9): p. 1905-1908.
32. Hinsen, K., *Analysis of domain motions by approximate normal mode calculations*. Proteins-Structure Function and Genetics, 1998. **33**(3): p. 417-429.
33. Atilgan, A.R. and L.S. Yilmaz, *Identifying the adaptive mechanism in globular proteins: Fluctuations in densely packed regions manipulate flexible parts*. Journal of Chemical Physics, 2000. **113**(10): p. 4454-4464.
34. Erman, B., *The Gaussian network model: Precise prediction of residue fluctuations and application to binding problems*. Biophysical Journal, 2006. **91**(10): p. 3589-3599.
35. Song, G. and R.L. Jernigan, *vGNM: A better model for understanding the dynamics of proteins in crystals*. Journal of Molecular Biology, 2007. **369**(3): p. 880-893.
36. Isin, B., et al., *Conformational changes of rhodopsin explored by using normal modes in steered molecular dynamics simulations*. Biophysical Journal, 2007: p. 20a-20a.
37. Bahar, I., P. Doruker, and A.R. Atilgan, *Dynamics of proteins predicted by molecular dynamics simulations and analytical approaches: Application to*

- alpha-amylase inhibitor*. Proteins-Structure Function and Genetics, 2000. **40**(3): p. 512-524.
38. Rader, A.J., et al., *Elastic network models reveal maturation dynamics of bacteriophage HK97*. Biophysical Journal, 2005. **88**(1): p. 232a-232a.
 39. Bahar, I., N.A. Temiz, and E. Meirovitch, *Escherichia coli adenylate kinase dynamics: Comparison of elastic network model modes with mode-coupling N-15-NMR relaxation data*. Proteins-Structure Function and Bioinformatics, 2004. **57**(3): p. 468-480.
 40. Bahar, I. and T. Haliloglu, *Structure-based analysis of protein dynamics: Comparison of theoretical results for hen lysozyme with X-ray diffraction and NMR relaxation data*. Proteins-Structure Function and Genetics, 1999. **37**(4): p. 654-667.
 41. Pande, V.S. and P. Petrone, *Can conformational change be described by only a few normal modes?* Biophysical Journal, 2006. **90**(5): p. 1583-1593.
 42. Jernigan, R.L., L. Yang, and G. Song, *How well can we understand large-scale protein motions using normal modes of elastic network models?* Biophysical Journal, 2007. **93**(3): p. 920-929.
 43. Dupuis, F., et al., *Voro3D: 3D Voronoi tessellations applied to protein structures*. Bioinformatics, 2005. **21**(8): p. 1715-1716.
 44. Csermely, P., et al., *Network analysis of protein dynamics*. Febs Letters, 2007. **581**(15): p. 2776-2782.
 45. Papila, M., E. Ozden, and Y.Z. Menciloglu, *Engineering Chemistry of Electrospun Nanofibers and Interfaces in Nanocomposites for Superior Mechanical Properties*. Acs Applied Materials & Interfaces, 2010. **2**(7): p. 1788-1793.
 46. Rong, M.Z., M.Q. Zhang, and W.H. Ruan, *Surface modification of nanoscale fillers for improving properties of polymer nanocomposites: a review*. Materials Science and Technology, 2006. **22**(7): p. 787-796.
 47. Coleman, J.N., et al., *Reinforcement of polymers with carbon nanotubes. The role of an ordered polymer interfacial region. Experiment and modeling*. Polymer, 2006. **47**(26): p. 8556-8561.
 48. Schulte, K., et al., *Influence of different carbon nanotubes on the mechanical properties of epoxy matrix composites - A comparative study*. Composites Science and Technology, 2005. **65**(15-16): p. 2300-2313.
 49. Torkelson, J.M. and C.J. Ellison, *The distribution of glass-transition temperatures in nanoscopically confined glass formers*. Nature Materials, 2003. **2**(10): p. 695-700.
 50. Kumar, S.K., et al., *Controlling the thermomechanical properties of polymer nanocomposites by tailoring the polymer-particle interface*. Journal of Polymer Science Part B-Polymer Physics, 2006. **44**(20): p. 2944-2950.
 51. Fisher, F.T., et al., *Reinforcement mechanisms in MWCNT-filled polycarbonate*. Composites Science and Technology, 2006. **66**(9): p. 1162-1173.
 52. Schadler, L.S., B.J. Ash, and R.W. Siegel, *Glass transition behavior of alumina/polymethylmethacrylate nanocomposites*. Materials Letters, 2002. **55**(1-2): p. 83-87.
 53. C. Becker, H.K., H. Schmidt. *Tailoring of thermomechanical properties of thermoplastic nanocomposites by surface modification of nanoscale silica particles*. in *Mat. Res. Soc. Symp. Proc.*
 54. Archer, L.A. and Q. Zhang, *Poly(ethylene oxide)/silica nanocomposites: Structure and rheology*. Langmuir, 2002. **18**(26): p. 10435-10442.

55. Mackay, M.E., et al., *Nanoscale effects leading to non-Einstein-like decrease in viscosity*. Nature Materials, 2003. **2**(11): p. 762-766.
56. Dutta, N.K., et al., *High-Resolution Solid-State Nmr Investigation of the Filler-Rubber Interaction .1. High-Speed H-1 Magic-Angle-Spinning Nmr-Spectroscopy in Carbon-Black Filled Styrene-Butadiene Rubber*. Polymer, 1994. **35**(20): p. 4293-4299.
57. Vidal, A., et al., *High-resolution solid-state NMR investigation of the filler-rubber interaction: 2. High-speed [H-1] magic-angle spinning NMR spectroscopy in carbon-black-filled polybutadiene*. Polymer International, 2001. **50**(4): p. 387-394.
58. Starr, F.W., T.B. Schroder, and S.C. Glotzer, *Molecular dynamics simulation of a polymer melt with a nanoscopic particle*. Macromolecules, 2002. **35**(11): p. 4481-4492.
59. Vacatello, M., *Molecular arrangements in polymer-based nanocomposites*. Macromolecular Theory and Simulations, 2002. **11**(7): p. 757-765.
60. Vacatello, M., *Monte Carlo simulations of polymer melts filled with solid nanoparticles*. Macromolecules, 2001. **34**(6): p. 1946-1952.
61. Starr, F.W., T.B. Schroder, and S.C. Glotzer, *Effects of a nanoscopic filler on the structure and dynamics of a simulated polymer melt and the relationship to ultrathin films*. Physical Review E, 2001. **64**(2).
62. Bitsanis, I. and G. Hadziioannou, *Molecular-Dynamics Simulations of the Structure and Dynamics of Confined Polymer Melts*. Journal of Chemical Physics, 1990. **92**(6): p. 3827-3847.
63. Baschnagel, J. and K. Binder, *On the Influence of Hard Walls on Structural-Properties in Polymer Glass Simulation*. Macromolecules, 1995. **28**(20): p. 6808-6818.
64. Baschnagel, J. and K. Binder, *Interfacial properties of glassy polymer melts: A Monte Carlo study*. Macromolecular Symposia, 1996. **106**: p. 41-54.
65. Hergeth, W.D., et al., *Polymerization in the Presence of Seeds .4. Emulsion Polymers Containing Inorganic Filler Particles*. Polymer, 1989. **30**(2): p. 254-258.
66. Yoshimoto, K., et al., *Local dynamic mechanical properties in model free-standing polymer thin films*. Journal of Chemical Physics, 2005. **122**(14).
67. Lequeux, F., et al., *Evidence for the shift of the glass transition near the particles in silica-filled elastomers*. Macromolecules, 2002. **35**(26): p. 9756-9762.
68. Berriot, J., et al., *Gradient of glass transition temperature in filled elastomers*. Europhysics Letters, 2003. **64**(1): p. 50-56.
69. Berman, H.M., et al., *The Protein Data Bank*. Nucleic Acids Research, 2000. **28**(1): p. 235-242.
70. Accelrys, I., *Materials Studio*. 2002: San Diego.
71. McQuarrie, D.A., *Statistical Mechanics*. 2000, Davis, USA: University Science Books.
72. Gee, R.H. and R.H. Boyd, *Conformational Dynamics and Relaxation in Bulk Polybutadienes - a Molecular-Dynamics Simulation Study*. Journal of Chemical Physics, 1994. **101**(9): p. 8028-8038.
73. *Materials Studio 4.4*. 2002, Accelrys Inc.: San Diego, USA.
74. Schulten, K., et al., *Scalable molecular dynamics with NAMD*. Journal of Computational Chemistry, 2005. **26**(16): p. 1781-1802.

75. Smith, G.D. and W. Paul, *United atom force field for molecular dynamics simulations of 1,4-polybutadiene based on quantum chemistry calculations on model molecules*. Journal of Physical Chemistry A, 1998. **102**(7): p. 1200-1208.
76. Kanaya, T., T. Kawaguchi, and K. Kaji, *Local Dynamics of Cis-1,4-Polybutadiene near the Glass-Transition Temperature-Tg*. Physica B-Condensed Matter, 1992. **182**(4): p. 403-408.
77. Wales, D.J., *The Cambridge Cluster Database*.
78. Poupon, A., *Voronoi and Voronoi-related tessellations in studies of protein structure and interaction*. Current Opinion in Structural Biology, 2004. **14**(2): p. 233-241.
79. Casadio, R. and P. Fariselli, *A neural network based predictor of residue contacts in proteins*. Protein Engineering, 1999. **12**(1): p. 15-21.
80. Atilgan, A.R., D. Turgut, and C. Atilgan, *Screened nonbonded interactions in native proteins manipulate optimal paths for robust residue communication*. Biophysical Journal, 2007. **92**(9): p. 3052-3062.
81. Varadarajan, R. and S. Chakravarty, *Residue depth: a novel parameter for the analysis of protein structure and stability*. Structure with Folding & Design, 1999. **7**(7): p. 723-732.
82. Bahar, I., Z. Bagci, and R.L. Jernigan, *Residue packing in proteins: Uniform distribution on a coarse-grained scale*. Journal of Chemical Physics, 2002. **116**(5): p. 2269-2276.
83. Baysal, C. and A.R. Atilgan, *Relaxation kinetics and the glassiness of proteins: The case of bovine pancreatic trypsin inhibitor*. Biophysical Journal, 2002. **83**(2): p. 699-705.
84. Baysal, C., et al., *Local dynamics of bulk polybutadienes of various microstructures: Comparison of theory with NMR measurements*. Macromolecules, 1997. **30**(7): p. 2058-2066.
85. Ghirelli, F. and B. Leckner, *Transport equation for the local residence time of a fluid*. Chemical Engineering Science, 2004. **59**(3): p. 513-523.
86. Theodorou, D.N. and U.W. Suter, *Atomistic Modeling of Mechanical-Properties of Polymeric Glasses*. Macromolecules, 1986. **19**(1): p. 139-154.
87. *Supplementary Notes of Materials Studio Program*, Accelerlys Inc.: San Diego, USA.
88. Levine, I.R., *Physical Chemistry*. 3rd ed. 1988, New York, USA: McGraw-Hill.
89. Stevens, M.P., *Polymer Chemistry: An Introduction*. 3rd ed. 1999, New York, USA: Oxford University Press.
90. Karplus, M., Y.Q. Zhou, and D. Vitkup, *Native proteins are surface-molten solids: Application of the Lindemann criterion for the solid versus liquid state*. Journal of Molecular Biology, 1999. **285**(4): p. 1371-1375.
91. ben-Avraham, D., *Vibrational Normal-Mode Spectrum of Globular-Proteins*. Physical Review B, 1993. **47**(21): p. 14559-14560.
92. Kittel, C., *Introduction to Solid State Physics*. International 8th ed. 2004: John Wiley & Sons.
93. Svanidze, A.V., et al., *Inelastic incoherent neutron scattering in some proteins*. Ferroelectrics, 2007. **348**: p. 556-562.
94. Reuveni, S., R. Granek, and J. Klafter, *Proteins: Coexistence of stability and flexibility*. Physical Review Letters, 2008. **100**(20).
95. Vulpiani, A., et al., *Topological thermal instability and length of proteins*. Proteins-Structure Function and Bioinformatics, 2004. **55**(3): p. 529-535.

96. Rodgers, P.A., *Pressure Volume Temperature Relationships for Polymeric Liquids - a Review of Equations of State and Their Characteristic Parameters for 56 Polymers*. Journal of Applied Polymer Science, 1993. **48**(6): p. 1061-1080.
97. DiBenedetto, A.T., *Molecular properties of amorphous high polymers. I. A cell theory for amorphous high polymers*. Journal of Polymer Science Part A: General Papers, 1963. **1**(11): p. 3459-3476.
98. Fetters, L.J., et al., *Connection between Polymer Molecular-Weight, Density, Chain Dimensions, and Melt Viscoelastic Properties*. Macromolecules, 1994. **27**(17): p. 4639-4647.
99. Fox, T.G. and P.J. Flory, *Second-order transition temperatures and related properties of polystyrene* Journal of Applied Physics, 1950(21): p. 581-591.
100. Baysal, C. and A.R. Atilgan, *Elucidating the structural mechanisms for biological activity of the chemokine family*. Proteins-Structure Function and Genetics, 2001. **43**(2): p. 150-160.
101. Ouyang, Z. and J. Liang, *Predicting protein folding rates from geometric contact and amino acid sequence*. Protein Science, 2008. **17**: p. 1256-1263.